Laser structuring of high mass loaded and aqueous acid processed $Li(Ni_{0.6}Mn_{0.2}Co_{0.2})O_2$ cathodes for lithium-ion batteries

Penghui Zhu [a,*], Vanessa Trouillet [b], Stefan Heißler [c], Wilhelm Pfleging [a]

[a] Institute for Applied Materials-Applied Materials Physics, Karlsruhe Institute of Technology, Hermann-von-Helmholtz-Platz 1, 76344 Eggenstein-Leopoldshafen, Germany

[b] Institute for Applied Materials-Energy Storage Systems and Karlsruhe Nano Micro Facility, Karlsruhe Institute of Technology, Hermann-von-Helmholtz-Platz 1, 76344 Eggenstein-Leopoldshafen, Germany

[c] Institute of Functional Interfaces, Karlsruhe Institute of Technology, Hermann-von-Helmholtz-Platz 1, 76344, Eggenstein-Leopoldshafen, Germany

Corresponding author: penghui.zhu@kit.edu

Abstract

Aqueous processing of cathode is a practical method to achieve cost reduction for lithium-ion batteries and provide environmentally friendly production by avoiding the use of the state-of-the-art polyvinylidene fluoride binder and toxic N-methyl-2-pyrrolidone solvent. However, the reaction of cathode materials with water leads to lithium leaching and a slurry pH value larger than 8. This results in chemical corrosion on current collector during coating process, leaving cavities inside dried electrodes. In this work, different acid additions were applied during mixing process in order to adjust slurry pH value. Besides, thick-film $Li(Ni_{0.6}Mn_{0.2}Co_{0.2})O_2$ cathodes were manufactured to achieve a high mass loading of about 35 mg/cm^2. X-ray photoelectron spectroscopy and Raman spectroscopy were applied to characterize the electrodes. Meanwhile, three-dimensional (3D) structures were generated in aqueous processed thick-film electrodes by applying ultrafast laser patterning and the active mass loss was adjusted to 7.5 %. Rate capability analyses, long-term performance, impedance spectroscopy, and cyclic voltammetry measurements were conducted to compare the electrochemical performance of cells with different cathode types. Rate capability analyses reveal that cells with structured aqueous processed thick electrodes with phosphoric acid and acetic acid show higher discharge capacity at specific current > 80 mA/g in comparison to ones with PVDF. Besides, cells containing structured high mass loaded electrodes with phosphoric acid maintain 72 % capacity, which is 15 % higher than the reference cells with PVDF.

1. Introduction

Lithium-ion batteries (LIBs) play a very important role in our daily life due to their extensive applications in energy storage, such as in stationary grid storage, portable devices, and electric power tools [1,2]. LIBs have developed rapidly since its first commercialization more than three decades ago and are occupying more market due to their high energy density in comparison to lead-acid, or Na-ion batteries [3,4]. With the rapid development of battery electric vehicles (BEV) and hybrid electric vehicles (HEV), the technical requirements for batteries, such as high capacity, high power, long calendar life, fast charging, low cost, and safety under extreme conditions, are more significant for the automobile industries [5–7]. In other words, batteries are the new "power train'' of electric vehicles.

Among the various cathode materials for LIBs, layered transition metal oxides $Li(Ni_xMn_yCo_{1-x-y})O_2$ (NMC), which are isostructural to α-$NaFeO_2$ [8], are very popular candidates for electric vehicles [9]. The specific capacity of NMC can be increased from 150 mAh/g to 200 mAh/g (or energy density over 300 Wh/kg at cell level) by increasing the Ni content in NMC materials [10–12], which is higher than that for other popular cathode materials such as $LiMn_2O_4$ (LMO), $LiFePO_4$ (LFP), and $LiCoO_2$ (LCO) [7]. During the electrode manufacturing, state-of-the-art polyvinylidene fluoride (PVDF) binder is usually

applied to maintain the mechanical integrity of electrodes by connecting active materials and/with conductive agents. However, conventional N-methyl-2-pyrrolidone (NMP) solvent used to disperse PVDF is toxic, expensive, volatile, and is thus difficult for an environmentally friendly electrode recycling [13]. Thus, eliminating NMP during cathode manufacturing benefits cost reduction of LIBs while reducing the environmental pollution. Water-based processing shows great potential owing to its low cost, short drying time, as well as safe production line without explosion hazard [14,15].

Aqueous processing of graphite anode has already become a standard procedure in battery industries and is further developed with addition of silicon in order to increase the energy density [16,17]. As for cathode materials, aqueous processing was firstly introduced by Li et al. [18] for LCO in 2007 and gained increasing attention in the past decade. Electrode manufacturing using water-based binders such as carboxymethyl cellulose (CMC), fluorinated acrylate polymer latex (TRD), alginate (ALG), polyacrylic acid (PAA), and guar gum (GG) for different cathode materials ranging from LFP [19,20], NMC [21–30], to high-voltage materials $LiNi_{0.5}Mn_{1.5}O_2$ (LNMO) [31] were studied. However, the major concern of water-based processing is the reactivity of active materials upon contacting with water, which results in material modification and respective phase transitions at the active materials surface [32], the formation of lithium carbonate and lithium hydroxide [33–35], as well as the dissolution of transition metal ions from cathode materials [36,37]. On the other hand, the lithium leaching mechanism results in slurry pH increase [38] and thus leads to chemical corrosion on aluminum current collector and hydrogen gas formation during coating process [39,40]. In general, three methods were introduced to counteract these effects: (i) using cathode materials coated with carbon, Al_2O_3, or Nb_2O_5 [41,42], (ii) providing carbon-coating on aluminum current collector to interdict its contact with alkaline slurry [43,44], and (iii) adjusting slurry pH with acid addition during mixing process [18,26,28,45]. The first two approaches involve additional processing steps, resulting in increased production costs, while the third method provides a feasible solution to the aqueous processing of cathode materials.

Using thick-film electrode with high mass loading is a practical strategy to increase the energy density of LIBs, since less inactive materials as current collector and separator are needed [14]. However, cells with thick-film electrodes show serious deterioration in the electrochemical performance, exhibiting low capacity retention at C-rates > C/5. This is mainly due to the accumulation of cell polarization, lithium-ion diffusion limitation, and local material degradation, which results in an increase of charge transfer resistance [46]. 3D battery concept with architectures generated by ultrafast laser ablation is proven to be beneficial to improve lithium-ion diffusion kinetics in thick-film electrode and meanwhile provides accelerated electrolyte wetting owing to the capillary microstructures in electrodes [47–49]. Besides, cells with laser structured NMC electrodes show higher capacity retention after long-term cycling and provide higher capacity under fast charging and discharging over C/2 [50–53]. The same phenomenon was observed for thick-film LCO cathodes with line structures [54] and laser drilled LFP cathodes [55]. On the other hand, laser patterned graphite w/o silicon anodes with grids, lines, and drilling holes, show high capacity retention and capability at high C-rates [16,17,56–58]. All these researches have proved that laser processing is of great significance to improve battery performance, especially for cells with thick-film electrodes.

In our previous works, we have studied the effect of slurry pH value on the electrochemical performance of cells containing $Li(Ni_{0.6}Mn_{0.2}Co_{0.2})O_2$ (NMC 622) cathode and found that the slurry pH value should be adjusted to 9-10 in order to mitigate the chemical corrosion between alkaline slurry and current collector. Meanwhile this pH range is essential to meet a suitable precondition for subsequent laser processing [59]. In this work, aqueous processing of NMC 622 cathode is further studied using different acid addition and the slurry pH values were kept at 9-10. X-ray photoelectron spectroscopy (XPS) and Raman spectroscopy were performed to characterize the NMC 622 electrodes manufactured with different acid addition in comparison to electrode with PVDF binder. Besides, the electrodes were patterned using ultrafast laser ablation to improve the electrochemical performance. Rate capability and long-term cycling on coin cells containing electrodes with state-of-the-art thickness (70 µm) and thick-film (150 µm) were conducted to study the effect of acid addition and laser patterning on the electrochemical performance. Furthermore, cyclic voltammetry electrochemical as well as impedance spectroscopy were applied to

investigate the lithium-ion diffusion and impedance of cells with unstructured and laser structured thick-film electrodes.

2. Experimental

2.1. Slurry preparation and electrode manufacturing

For reference electrodes with PVDF binder, commercially available NMC 622 powder with a particle size D90 of 12.8 µm (BASF SE, Germany) was used as active material, while C-NERGY Super C65 (Imerys Graphite & Carbon, Belgium) and C-NERGY KS6L graphite (Imerys Graphite & Carbon, Switzerland) were applied as conductive agent and compaction aid, respectively. Solef 5130 PVDF powder (Solvay, Germany) was dissolved in NMP (Merck, Germany) with a mass ratio of 1:10 in advance, while other powders were added into PVDF solvent with NMC 622: Super C65: KS6L graphite: PVDF powder = 92: 3: 2: 3 (wt. %). The slurry was mixed in a planetary mixer (SpeedMixer DAC 150 SP, Hauschild & Co. KG, Germany) for 1.5 h with 1500-3500 rpm, and extra NMP solution was added into the mixture in order to adjust the slurry viscosity. The solid content of electrode slurry was 66.7 wt. % by the end of mixing process.

For aqueous slurry preparation, same NMC 622 powder as well as C-NERGY Super C65 were applied, while Na-CMC (CRT 2000PA, Dow Wolff Cellulosic, Germany) and fluorine acrylic copolymer latex TRD 202A (40 wt. % solution, JSR Micro NV, Belgium) were used as thickening agent and binders, respectively. Before slurry preparation, Na-CMC powder was dissolved in DI water and mixed in a dissolver (VMA-Getzmann, Germany) with 1500 rpm for 1 h to acquire a 5 wt. % CMC solvent. Afterwards, NMC 622 powder and Super C65 carbon black were mixed together and added into the CMC solvent, while the container was persistently water-cooled to 20 °C. Subsequently, one of the acids, which were either phosphoric acid in 85 wt. % solution (Sigma-Aldrich, USA), 100 % liquid acetic acid (Merck, Germany), or monohydrate citric acid (Merck, Germany), was added into the slurry to adjust the slurry pH value to 9-10. The slurry was afterwards stirred at 2000 rpm for 90 min to disperse the carbon black and NMC 622 powder homogenously. At the end, shear sensitive latex binder TRD 202A was added into the slurry and the slurry was subsequently mixed at 500 rpm for 3 min under vacuum. The mass ratio of each constituent is NMC 622: Super C65: Na-CMC: TRD 202A = 92.6: 2.8: 0.8: 2.8. The slurry pH values were measured 15 min after the mixing procedure was finished using a pH-meter (FE30-Basic FiveEasy, Mettler-Toledo GmbH, Germany).

The NMP or aqueous based slurry was tape-cast with a doctor blade (ZUA 2000.100, Proceq, Switzerland) onto an aluminum foil with 20 µm thickness, which was placed on a tape coater (MSK-AFA-L800-LD, MTI Corporation, USA) and was fixed on a vacuum table. The coating speed was 5 mm/s while the electrode wet film thickness was controlled by varying the gap of doctor blade. The aqueous slurry was dried at room temperature for 1 h while the NMP-based slurry was dried at 90 °C for 2.5 h. After drying, the electrodes were calendered at room temperature using a rolling press (MSK-2150, MTI Corporation, USA) with a constant calendering speed of 35 mm/s. The porosity of electrodes with different acid addition as well as with PVDF binder was adjusted to 35 %. The porosity was determined by the weight percent and density of each component [50,60]. Two different thicknesses at around 70 µm and 150 µm (after calendering) were chosen to represent the state-of-the-art thickness and thick-film electrode, respectively.

2.2. Laser processing

A fiber laser (Tangerine, Amplitude Systèmes, France) operating at a wavelength of 515 nm ($M^2 < 1.3$) and a pulse duration of 380 femtoseconds (fs) was used to pattern electrodes with 150 µm thickness. A repetition rate of 500 kHz and an average laser power of 2.5 W were applied, while the laser scanning speed

was kept constant at 500 mm/s. The laser scan passes were about 15 to 16 with regard to the cathodes with different binder and acid addition. Since cathode material takes up about 50 % of the overall material costs in a LIB [61], the mass loss due to laser ablation must be adjusted to values of < 10 %, which means the structured grooves should be as narrow as possible. In this study, line structures with 200 µm pitch were generated in thick-film electrodes. Cross-sectional analyses using an optical Leica microscope were applied to determine the width and depth of the groove structures. Besides, the electrodes for coin cell design were then laser cut in 12 mm circles using an average laser power of 5 W and a laser scan speed of 200 mm/s. All types of laser processing were performed in ambient air.

2.3. Electrode characterization

Scanning electron microscopy (SEM, Phenom XL, Thermo Scientific, USA) with 10 kV accelerating voltage was used to investigate the effect of different acids on the morphology of electrode materials and to study a possible thermal impact of laser processing.

X-ray photoelectron spectroscopy (XPS) analysis of NMC 622 cathodes with different acid addition during slurry preparation was performed with a K-alpha spectrometer (ThermoFisher Scientific, UK). Thermo Avantage software was used for data acquisition and processing. All samples were analyzed using a micro-focused, monochromated Al Kα X-ray source (400 µm spot size). The K-Alpha charge compensation system was employed during analysis using electrons of 8 eV energy and low-energy argon-ions to prevent any localized charge build-up. The spectra were fitted with one or more Voigt profiles (BE uncertainty: ± 0.2 eV) and Scofield sensitivity factors were applied for the quantification [62]. All spectra were referenced to the C 1s graphitic peak (sp^2) at 284.4 eV binding energy controlled by means of the well-known photoelectron peaks of metallic Cu, Ag, and Au, respectively.

A Raman microscope (Senterra II, Bruker Optics, Germany) equipped with a DPSS laser operating at 532 nm wavelength was applied. For the observation of the sample surface, focusing and collimation of backscattered light, an Olympus MPLAN 20 x objective (NA 0.45) was used, resulting in a spot diameter of 5 µm at sample surface. The spectra integration time was 40 s with four coadditions (4*10 s). The laser power was set to 6 mW and 2.5 mW for the detection of electrodes and pristine NMC 622 powder, respectively. For each sample, the spectra were recorded with a bandwidth ranging from 75 to 4000 cm^{-1} at 8 to 10 randomly selected locations.

2.4. Electrochemical analyses

All electrodes were dried at 130 °C for 12 h under vacuum prior to cell assembly. Then they were transferred to an argon-filled glove box (LAB master pro sp, M. Braun, Germany) with H_2O< 0.1 ppm and O_2< 0.1 ppm, and were assembled versus lithium foil (Merck, Germany) with a thickness of 0.25 mm in CR2032 coin cell. A total amount of 120 µl electrolyte, which consists of 1.3 M $LiPF_6$ in ethylene carbonate (EC) and ethyl methyl carbonate (EMC) with EC: EMC = 3: 7 (vol. %) plus 5 wt. % of fluoroethylene carbonate (FEC) additive, was added to each cell. A polypropylene (PP) separator foil (Celgard 2500, USA) with a thickness of 25 µm was placed between NMC 622 cathode and lithium. All cell components were pressed using an electric crimper (MSK-160D, MTI Corporation, USA) after stacking and the cells were stored at room temperature for 24 h to enable a complete wetting of separator and cathode.

Rate capability analyses were carried out using a battery cycler (BT2000, Arbin Instruments, USA). During charging, ‘‘constant current-constant voltage’’ (CCCV) method was applied for each C-rate, while constant current (CC) was used for discharging. The upper and lower cut-off voltages were 4.3 and 3.0 V, respectively. At the beginning, 3 cycles at C/20 were performed as formation step, followed by increasing C-rates from C/10 to 5C. Finally, 5 cycles at C/5 were applied to study a possible capacity loss due to rate capability measurement. Besides, symmetrical protocol was applied for rate capability test, which means

currents for charging and discharging were the same. After rate capability test, cells were cycled at C/2 for 100 cycles to study the long-term performance and degradation.

Electrochemical impedance spectroscopy (EIS) was conducted after rate capability analyses to determine the impedance of coin cells containing different electrode types. A potentiostat (VMPS, Biologic, France) was used to perform EIS analyses on cells at the open circuit voltage (OCV) at around 3.6 V, while the cells were placed in an oven with a constant temperature of 25 °C. The scanning frequency of EIS analyses ranged from 0.02 Hz to 1 MHz, while a sinus amplitude of 10 mV was applied. ZView 2 (Scribner Associates Inc.) software was employed to fit the EIS data to an equivalent electronic circuit.

In order to determine the redox reaction and to calculate the effective lithium-ion diffusion coefficient, cyclic voltammetry (CV) measurement was performed after the formation step using a battery cycler (BCS-810, Biologic, France). Scan rates ranging from 0.02 to 0.12 mV/s with 0.02 mV/s increment were applied, while the voltage window was set from 3.0 to 4.3 V.

3. Results and discussion

3.1 Electrode manufacturing and the effect of acid addition on NMC 622 properties

During the mixing process, acid was added into the slurry to adjust the slurry pH value to 9-10. According to our previous study, no cavities owing to hydrogen generation were observed in dried electrode when the slurry pH was set to values < 10 [59]. Furthermore, researches on pH modification with different acid types showed that the electrochemical performance of cell with aqueous processed cathode deteriorates when the slurry pH value is < 9 [26,30,59]. The amount of acid, the slurry pH value as well as the details of different electrodes are given in Table 1. The active mass loading is related to the active material NMC 622 in the electrode. With increasing film thickness, the mass loading of NMC 622 cathodes increases from 17 mg/cm^2 to about 34-38 mg/cm^2, which is almost twice higher compared to electrodes with state-of-the-art thickness. For the calculation of areal capacity, specific capacities of 172 mAh/g and 166 mAh/g were applied for PVDF-based and aqueous processed NMC 622 electrodes, respectively. This is due to the hydrolysis of NMC 622 during mixing process, which results in the exchange of lithium-ions from the surface of active material with protons in electrolyte [32]. The lithium-leaching leads to a lower capacity of NMC 622 in aqueous processed electrodes.

Table 1. The amount of acid, slurry pH value, film thickness, active mass loading, and areal capacity of NMC 622 electrodes with different type of binder or acid addition.

Electrode type	Acid amount (wt. %)[1]	Slurry pH[2]	Film thickness (µm)	Active mass loading (mg/cm^2)	Areal capacity (mAh/cm^2)
Reference with PVDF	-	-	74 ± 2	18.8 ± 0.2	3.2 ± 0.1
With citric acid (CA)	2.3	9.3	73 ± 2	17.0 ± 0.1	2.8 ± 0.1
With acetic acid (AA)	1.4	9.4	71 ± 2	16.1 ± 0.2	2.7 ± 0.1
With phosphoric acid (PA)	0.9	9.5	73 ± 2	16.9 ± 0.3	2.8 ± 0.1
Reference with PVDF	-	-	150 ± 5	36.9 ± 0.9	6.4 ± 0.2
With citric acid (CA)	2.3	9.3	160 ± 6	38.9 ± 1.4	6.5 ± 0.2

With acetic acid (AA)	1.4	9.4	149 ± 4	33.9 ± 0.2	5.6 ± 0.1
With phosphoric acid (PA)	0.9	9.5	149 ± 4	35.3 ± 0.3	5.9 ± 0.1

[1] The acid amount is calculated by dividing the mass of acid by the mass of NMC 622.
[2] The slurry pH values were measured 5 min after the slurry mixing was completed.

The SEM images of different types of NMC 622 electrodes are shown in Figure 1. In Figure 1-a, it is found that the NMC 622 particles are homogenously covered with PVDF binder, while the flake-like KS6L graphite distributes between NMC particles. Due to the high apparent density and compressibility of KS6L graphite, the direct contact between NMC 622 particles and the contact between NMC 622 and conductive agents are improved, thus leads to a lower electrical resistivity [63]. The conductive agent Super C65 has a primary particle diameter < 50 nm [64], which is beyond the resolution of SEM. However, in Figure 1-b and -d, conductive agent on the NMC surface and the agglomerated ones between NMC particles can be observed. The small particles in the slurry can help to unfold the CMC polymer coils during mixing and thus leads to extended bridging between particles [26]. In Figure 1-c, the top view of the electrode shows cracks in some NMC 622 particles, which are assumed to be originated from the calendering process.

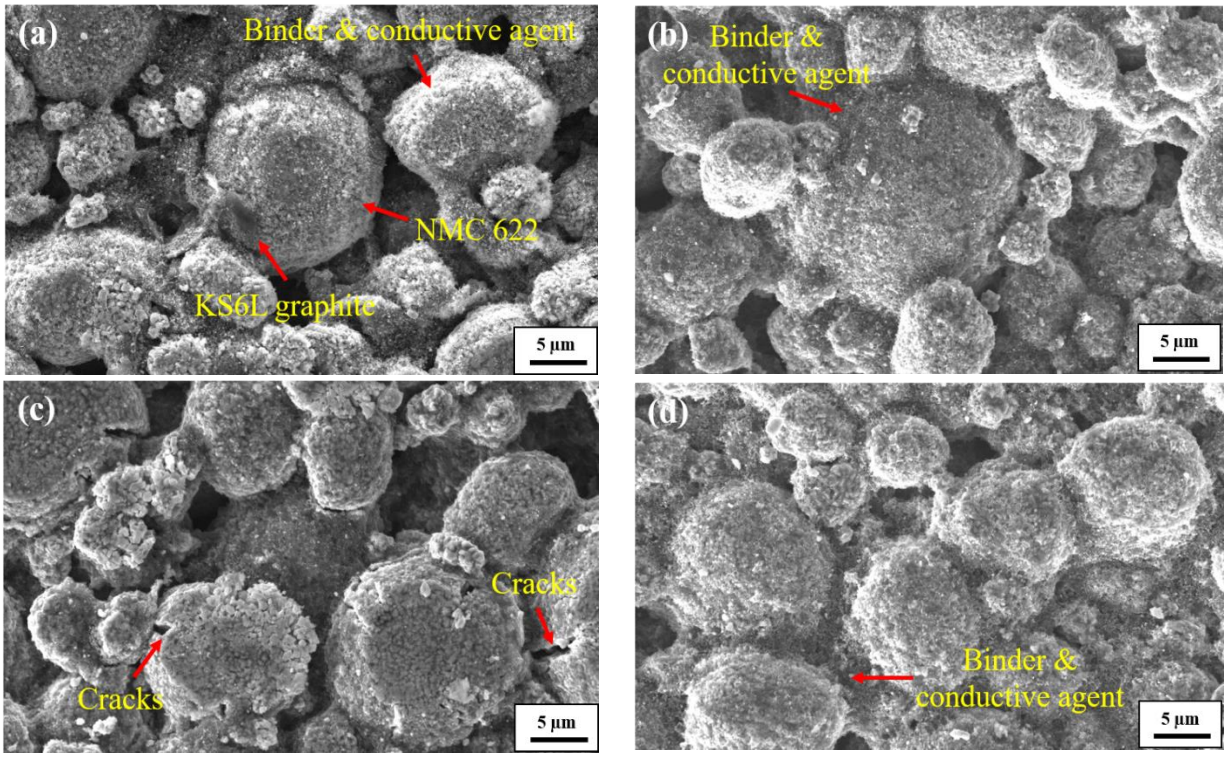

Figure 1. SEM images of (**a**) NMC 622 cathodes with PVDF binder and aqueous processed cathodes with addition of (**b**) citric acid, (**c**) acetic acid, and (**d**) phosphoric acid.

The surface chemical compositions of dried electrodes processed with different acid addition during slurry preparation as well as reference electrodes without acid addition or with PVDF binder were characterized using XPS analysis. In C 1s spectra (Figure 2-a), the peak at 284.4 eV is assigned to the carbon black (conductive agent) in electrodes, while the signal at 285.4 eV corresponds to C-C/C-H bonds. A very weak peak at 290.4 eV can be attributed to lithium carbonate species on the surface of NMC 622 [65]. It has been reported that Li_2CO_3 and LiOH are formed when NMC 622 powders are stored at room humidity over 80 % [35], thus it is assumed that more Li_2CO_3 would be generated on the NMC 622 surface by applying aqueous mixing process. However, a direct comparison between the amount of Li_2CO_3 in aqueous

processed electrodes with reference PVDF-based electrode is intractable, since the CF_2 peak, which is characteristic for PVDF in the reference electrode, overlaps with CO_3^{2-} peak at 290.4 eV, as shown in Figure 2-a. Besides, 0.2 at. % of CF_2 at 290.7 eV was detected in dried TRD 202A binder. However, since the amount of TRD 202A binder was kept the same in aqueous processed electrodes with different acid addition, the contribution of TRD 202A can be neglected. The trend of the Li_2CO_3 content in electrodes with addition of different acid can be followed by calculating the atomic ratio between the peak at 290.4 eV and carbon black peak at 284.4 eV, since the carbon black amounts in different aqueous processed electrodes remains the same. However, no obvious differences in Li_2CO_3 amount are observed between the different acid containing electrodes in comparison to reference electrode without acid addition, All contain a very low concentration of Li_2CO_3 (~ 1.1 at. %) detected on the NMC 622 surface, also the reference one. Therefore, it cannot be concluded that the acid addition results in a reduction of Li_2CO_3 on the NMC 622 surfaces.

Figure 2-b displays the P 2p spectra of different NMC 622 electrodes. A new peak appears at 133.3 eV for electrode with phosphoric acid addition and the atomic percent is about 0.3 %. This may indicate the formation of water-insoluble species such as Li_3PO_4 [45,66–68], or $M_3(PO_4)_2$ (M is transition metal) [69]. However, XPS spectra cannot reveal whether the phosphates are bound or absorbed to the NMC 622 surface. This will be further discussed along with results from electrochemical performance of cells containing different electrodes types. Besides, 2.4-2.7 at. % lithium is measured, which is distinctly higher than the corresponding Ni, Mn or Co atoms in NMC 622. This might be explained by the lithium leaching and re-deposition. According to the study from Hamam et al. [70], in solutions with pH value from 7-10, lithium-ions/proton exchange and transition metal ion dissolution occur in NMC 532, and the removal is accelerated when slurry pH value < 7. In this work, the slurry pH values were adjusted to 9-10. Therefore, lithium leaching happens during mixing process, and the lithium-ion concentration in water is increased in comparison to its amount on the surface of NMC 622. After drying process, with the elimination of water, the lithium-ions might deposit again on the surface of NMC 622, thus leads to higher lithium concentration on the NMC 622 surface.

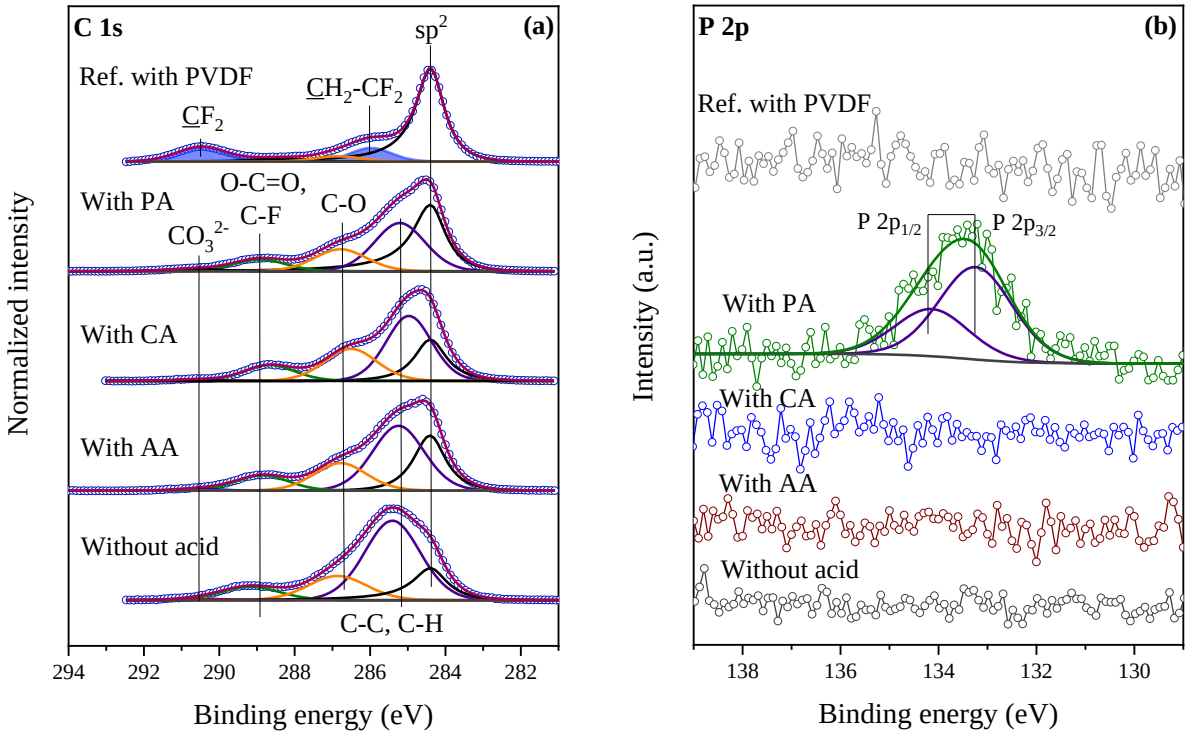

Figure 2. XPS spectra of the (a) C 1s and (b) P 2p lines of electrodes processed with different binders or with different acid addition during mixing.

The local structure of NMC 622 is investigated using Raman scattering, since Raman spectroscopy is sensitive to the short-range environment of oxygen around the cations in the lattice of an oxide [71]. Figure 3 compares the Raman spectra of NMC 622 cathodes processed with different acids as well as the spectrum of pristine NMC 622 powder and the spectrum of reference electrode with PVDF. The Raman active modes of NMC 622 particles are observed between 400 and 650 cm^{-1}, which are associated to the vibrational modes of different transition-metal-ions (Ni, Mn, Co). Two Raman-active modes, A_{1g} at around 570 cm^{-1} and E_g at around 470 cm^{-1} are detected for NMC 622 powder as well as electrodes processed with different acids, which represent oxygen-atoms moving symmetrically along the c-axis (M–O, M = Ni, Co, or Mn), and opposing oxygen-atoms displacements along adjacent oxygen layers (O–M–O), respectively [72]. Since A_{1g} represents stretching and is typically stiffer than bending mode, the band at higher wavenumber is usually assigned to A_{1g} [73]. From the work of C. Julien [74] it is found that with increasing Ni content in $LiNi_{1-x}Co_xO_2$, the A_{1g} band shifts from 600 cm^{-1} to lower wavenumber. In this work, the A_{1g} band of NMC 622 pristine powder locates at around 570 cm^{-1}, which is lower in comparison to other reports who show A_{1g} band at 609 cm^{-1} and 597 cm^{-1} [72,73]. The band shift may result from inhomogeneous polycrystalline, crystalline size and orientation, and the wavelength of excitation source [73]. The Raman spectra of NMC 622 electrodes and pristine NMC 622 powder are envelopes consist of highly overlapping bands of different transition-metal-ions, thus it is difficult to assign the exact band to each vibration mode. However, by comparing with different works it can be concluded that the bands > 600 cm^{-1} correspond to E_g and A_{1g} of Mn, while the shoulder at 465 cm^{-1} can be assigned to E_g mode of Ni. Between 470 and 590 cm^{-1}, the bands should in turn belong to E_g mode of Co, A_{1g} mode of Co, and A_{1g} of Ni with increasing wavenumber. Besides, the detection depth of Raman spectrum is in the range of several hundred nanometers, thus the intensity of A_{1g}/E_g can be used to determine the lithium leaching from NMC 622 surface in aqueous processed electrodes [35], since the A_{1g} band decreases fast with increasing lithium deintercalation [73]. The pristine NMC 622 powder and reference electrode with PVDF have an A_{1g}/E_g ratio of 2.4 – 2.5, while the aqueous processed electrodes with CA and AA show a lower ratio of 2.1 – 2.2, which indicates lithium leaching during mixing process. However, the electrode with PA displays an A_{1g}/E_g ratio of 2.5, which is higher in comparison to other aqueous processed electrodes. This further confirms the assumption that a protective layer is built on the NMC 622 surface with addition of phosphoric acid which can alleviate the lithium leaching during mixing process.

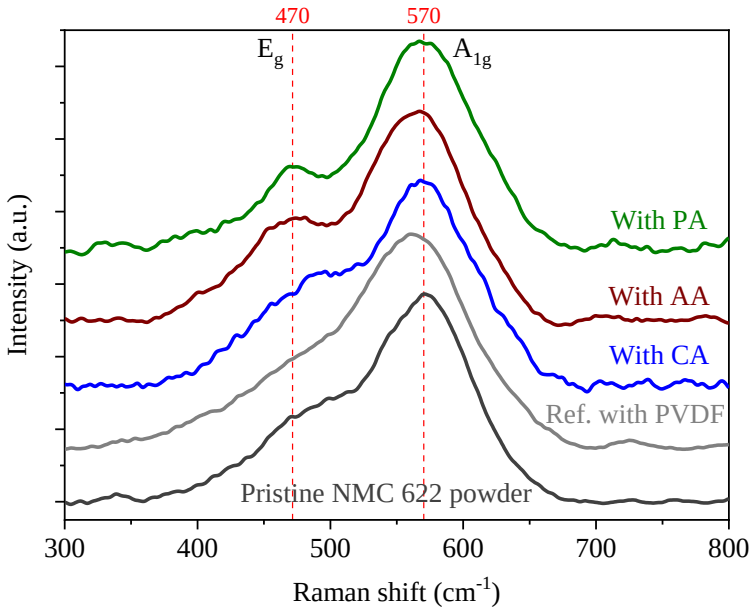

Figure 3. Raman spectra of NMC 622 electrodes processed with citric acid (CA), acetic acid (AA), phosphoric acid (PA), with PVDF binder, and pristine NMC 622 powder.

3.2 Laser structuring of aqueous processed cathodes

In order to determine the laser ablation depth in composite electrodes, cross section analyses of laser structured electrodes processed with different acid addition were performed, as shown in Figure 4. The slurry pH value was adjusted to 9-10 by adding acid during mixing process. Corrosion between slurry and Al current collector during coating was suppressed, thus no cavities with diameter larger than 50 µm owing to hydrogen generation are observed inside the dried electrode, which is consistent with our previous study [59]. The laser scan passes were adjusted to achieve channel structures reaching from the electrode surface down to the current collector, without damaging the current collector. The number of scan passes for different types of electrodes are similar (15-16 passes), indicating identical ablation behavior regardless of different acid addition. High resolution SEM images in Figure S1 show the edges of channels in structured electrodes. No melted particles or heat affected zone near the channels are observed. The direct sublimation of materials using ultrafast laser is beneficial to achieve microstructures with high aspect ratio and smooth surface. Besides, no new phases of the active material NMC 622 are formed during the ablation process, which has been proved by Dunlap et al. using X-ray diffraction (XRD) [53]. The channel structures inside electrodes can accelerate electrolyte wetting due to the capillary effect [49]. Meanwhile, electrolyte filled channels serve as electrolyte reservoir and can enhance the battery lifetime [50,59,75].

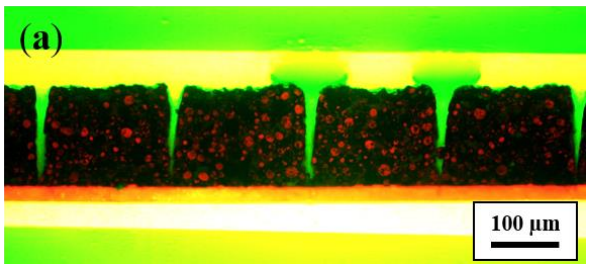

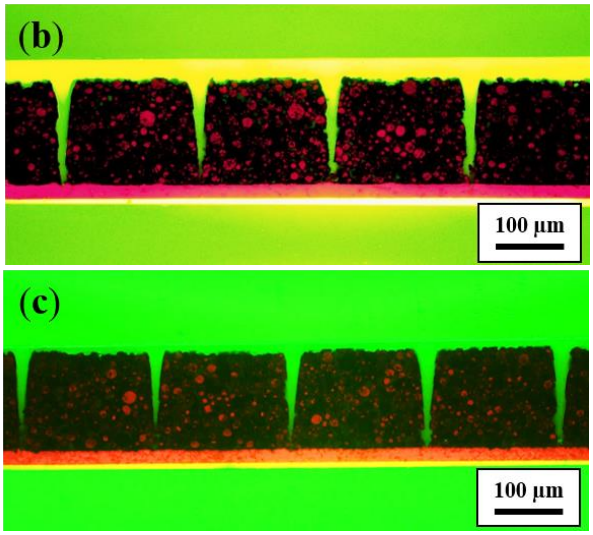

Figure 4. Cross-sectional view of laser structured and aqueous processed NMC 622 cathode with addition of (**a**) CA, (**b**) AA, and (**c**) PA during mixing process (average laser power: 2.5 W, repetition rate: 500 kHz, laser scan passes: 15-16).

Figure 4 shows that all channels have similar V-shape with wider opening at electrode surface. The geometric information of channels in structured electrodes and mass loss owing to laser structuring are summarized in Table 2. The mass loss is calculated from the weight difference between structured and unstructured electrodes from the same batch of electrode sheets, excluding the mass of the current collector. The top width of channels near the electrode surface is about 30 µm, which corresponds to Gaussian laser beam with a spot size of approximately 26 µm at focal length. For different types of electrodes, the mass loss is controlled at around 7.5 %, which is lower in comparison to results from Dunlap et al. [53] with 11.6 % and from Park et al. [52] with 13-20 %. Since cathode material is much more expensive than anode ones and other inactive components in a battery [61], lower mass loss is beneficial to maintain a high areal capacity while guaranteeing the advantages of laser structuring.

Table 2. Maximum width and full width at half maximum (FWHM) of the groove structures in different electrodes and the respective mass loss due to laser structuring.

Electrode type	Max. width (µm)	FWHM (µm)	Mass loss (%)
With CA	31.2 ± 3.8	12.6 ± 1.8	7.5 ± 4.8
With AA	32.7 ± 2.7	13.7 ± 0.3	7.5 ± 2.7
With PA	29.8 ± 3.0	14.9 ± 0.4	7.4 ± 1.5

3.3 Electrochemical performance of cells

In this chapter the electrochemical performance of cells containing unstructured and structured NMC 622 cathodes will be presented and discussed with respect to acid addition in comparison to reference cells containing NMC 622 cathode using PVDF as binder.

3.3.1 Rate capability analyses

The discharge capacities of cells with different types of NMC 622 cathodes at C-rates ranging from C/20 to 5C are shown in Figure 5. At least 3 cells were measured for each cell type and the average specific discharge capacities were plotted. After cell assembly each cell was cycled 3 times at C/20 in order to establish a stable cathode electrolyte interphase (CEI) [76]. The cells containing electrodes with PVDF binder and with acetic acid achieve a specific capacity of about 175-178 mAh/g, while the cells containing

cathodes with citric acid and phosphoric acid provide about 170 mAh/g specific capacity after formation. Coulombic efficiencies (CE) of cells containing electrodes processed with different acid at the first C/20 formation step are listed in Table 3. For cells with thin-film electrodes, the CE of reference cells with PVDF binder is 1-2 % higher in comparison to cells with aqueous processed electrodes. A lower CE at the first cycle indicates an increased electrolyte consumption to form the CEI during charging/discharging [28], which might be resulted from a rougher surfaces of NMC 622 powders after acid treatment, where reaction products were deposited [45]. Cells with aqueous processed thick-film electrodes show almost the same CE at the first cycle as those with thin-film electrodes, which are similar to the result from Kukay et al. [28] using full cells containing phosphoric acid treated NMC 811 cathodes and graphite anodes. As for cells with laser structured electrodes, it is found that the first cycle CE is about 2 % lower, which should be owing to formation of CEI on the generated channel surface between electrolyte and electrode after laser structuring. After the first cycle, the CE rises to 99-100 % for all cells at C/20, which implies adequate CEI formation on NMC 622 electrode.

Table 3. Coulombic efficiency of cells containing different types of electrodes at the first cycle by the formation.

	Coulombic efficiency at the first cycle (%)		
Electrode type	Thin-film	Thick-film (unstructured)	Thick-film (structured)
With CA	88.6	88.9	86.5
With AA	89.5	90.1	88.2
With PA	87.5	86.5	86.2
Ref. with PVDF	90.0	88.5	-

Figure 5-a displays that for cells with unstructured thin-film electrodes, the reference cells containing cathodes with PVDF binder show higher capacity from C/10 to 2C in comparison to cells with aqueous processed cathodes. For example, at C/10, the reference cells show 175 mAh/g specific capacity, while cells with aqueous processed electrodes provide about 165-170 mAh/g specific capacity, which is similar to prior reported results [38]. The capacity losses of cells containing electrodes with addition of CA and AA are more pronounced with increasing C-rates from C/2 to 3C in comparison to ones with PA or with PVDF. At 2C, the reference cells and cells containing electrode with PA maintain 65 mAh/g and 52 mAh/g specific capacity, respectively, while cells containing electrodes with CA and AA drop to 15 mAh/g at the 10^{th} cycle of 2C. At 3C, cells with CA and with AA show 5 mAh/g specific capacity, while cells with other two types of electrode still achieve about 30 mAh/g capacity. After fast charging and discharging, the cells were again cycled 5 times at C/5 to determine the cell degradation. Reference cells as well as cells containing electrode with PA retain the same capacity compared to previous C/5, while cells with CA and with AA reach 86 % and 89 % capacity after being cycled at high C-rates. With the addition of PA during slurry preparation, not only the slurry pH value is lower, but it might leads to the formation of transition metal phosphate, Li_3PO_4, or Li_2HPO_4 layer at the surface NMC 622 particles as shown in the P 2p spectra from XPS analysis in Figure 2, which is evidenced by other researches using NMC 111 as active material [68]. Jo et al. [77] also showed that the electrodes with PA modified NMC 622 exhibit high capacity retention. However, in their study the NMC 622 powders were pre-modified in PA solution and heated at 500 °C prior to slurry preparation and conventional PVDF binder was used for the electrode manufacturing.

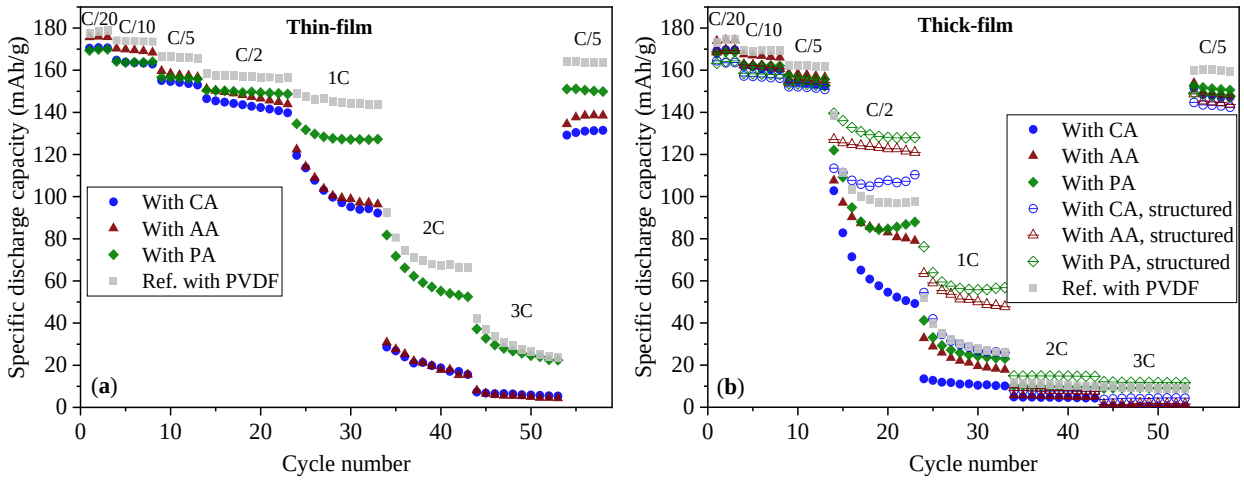

Figure 5. Specific discharge capacity of cells containing (**a**) electrodes with 70 µm thickness and (**b**) electrodes with 150 µm thickness with increasing C-rates from C/20 to 3C. For each electrode film thickness, three different acids were added during the mixing process of NMC 622 electrode.

The rate capabilities of cells with thick-film electrodes are depicted in Figure 5-b. At C/20 and C/10, cells with structured electrodes reveal 5 mAh/g less capacity in comparison to those with unstructured electrodes. At C/5 all cells exhibit similar capacities of 155 mAh/g except cells with PVDF, whose capacities are 5 mAh/g higher. When the C-rate increases to C/2, cells with laser structured electrodes start to show superior performance. Cells containing structured PA electrode retain the highest specific capacity of 130 mAh/g, followed by cells with structured AA and CA electrodes with 125 mAh/g and 106 mAh/g, respectively. Besides, all cells with structured aqueous processed electrodes exhibit higher specific capacity in comparison to reference cells with conventional PVDF binder. For example, cells with structured PA electrode show 31 mAh/g and 26 mAh/g higher discharge capacity at C/2 and 1C (32 % and 87 % higher) in comparison to reference cells, respectively. From rate capability analyses it is found that for cells with thick-film electrodes, both phosphoric acid and acetic acid are good candidates to improve the electrochemical performance of NMC 622 in combination with laser structuring, especially at C-rates ≥ C/2.

Discharge profiles of cells containing different types of thick-film electrodes from the last C/10 and C/2 cycles are presented in

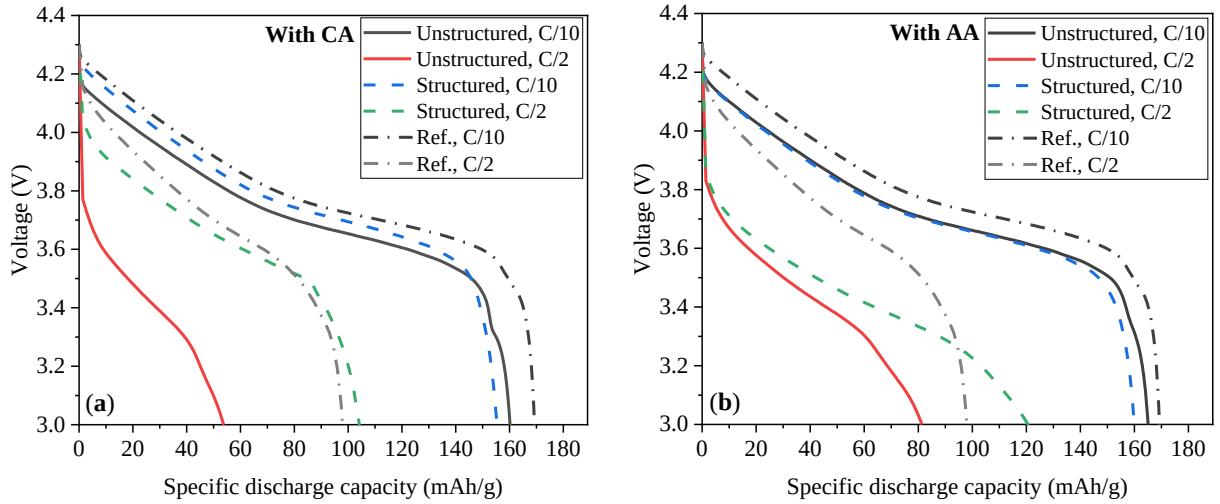

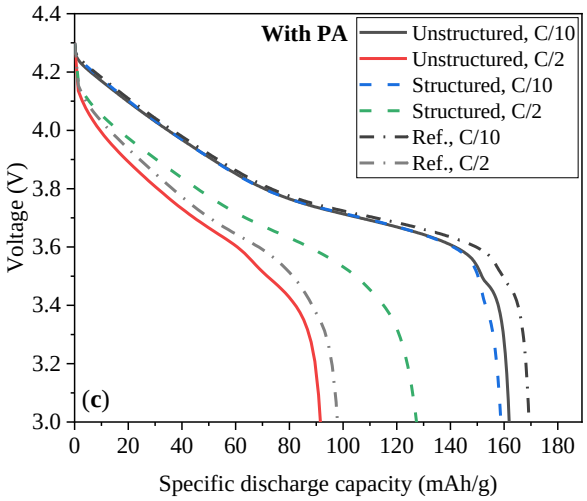

Figure 6. At C/10, the discharge capacities of cell with AA and reference cell with PVDF reach about 165 mAh/g, while the cells with CA and PA show 5 mAh/g lower capacity. Meanwhile, cells with structured electrodes exhibit about 3-5 mAh/g less capacity at C/10 in comparison to ones with unstructured electrodes. When we observe the "IR-drop", which refers to the linear voltage drop at the beginning of the discharge curve, we can find that the IR drop of cells with CA and AA (from 4.3 V to < 4.2 V) is higher in contrast to cell with PA and PVDF (from 4.3 V to 4.25 V). This indicates a higher ohmic resistance for the first two types of electrodes. However, for cells with CA, it is found that after laser structuring, the IR-drop is decreased. Besides, the discharge plateau of cells with structured electrode with CA is higher in comparison to ones with unstructured electrodes, indicating a lower cell polarization. But no difference is found in the discharge profiles of cells containing electrode with AA and PA with/without laser structuring. When C-rate increases to C/2, IR-drop of cells with CA and AA increases (from 4.3 V to 3.8 V), while cells with other two kinds of electrodes show lower IR-drop from 4.3 V to 4.15 V. On the other side, all cells with structured electrodes display lower cell polarization from 4.3 V to 3.5 V at C/2 in comparison to those with unstructured electrodes. In several studies it was shown that the energy density increases with increasing electrode thickness and lower porosity, while power density is dramatically reduced [47,48,78]. In this work, the channel structures generated due to laser ablation provide extra porosity in electrodes, while the unstructured parts remain a low porosity and a high thickness. Therefore, in contrast to cells with unstructured electrodes, laser structuring can compensate the power density drop in cells with thick-film electrodes at high C-rates.

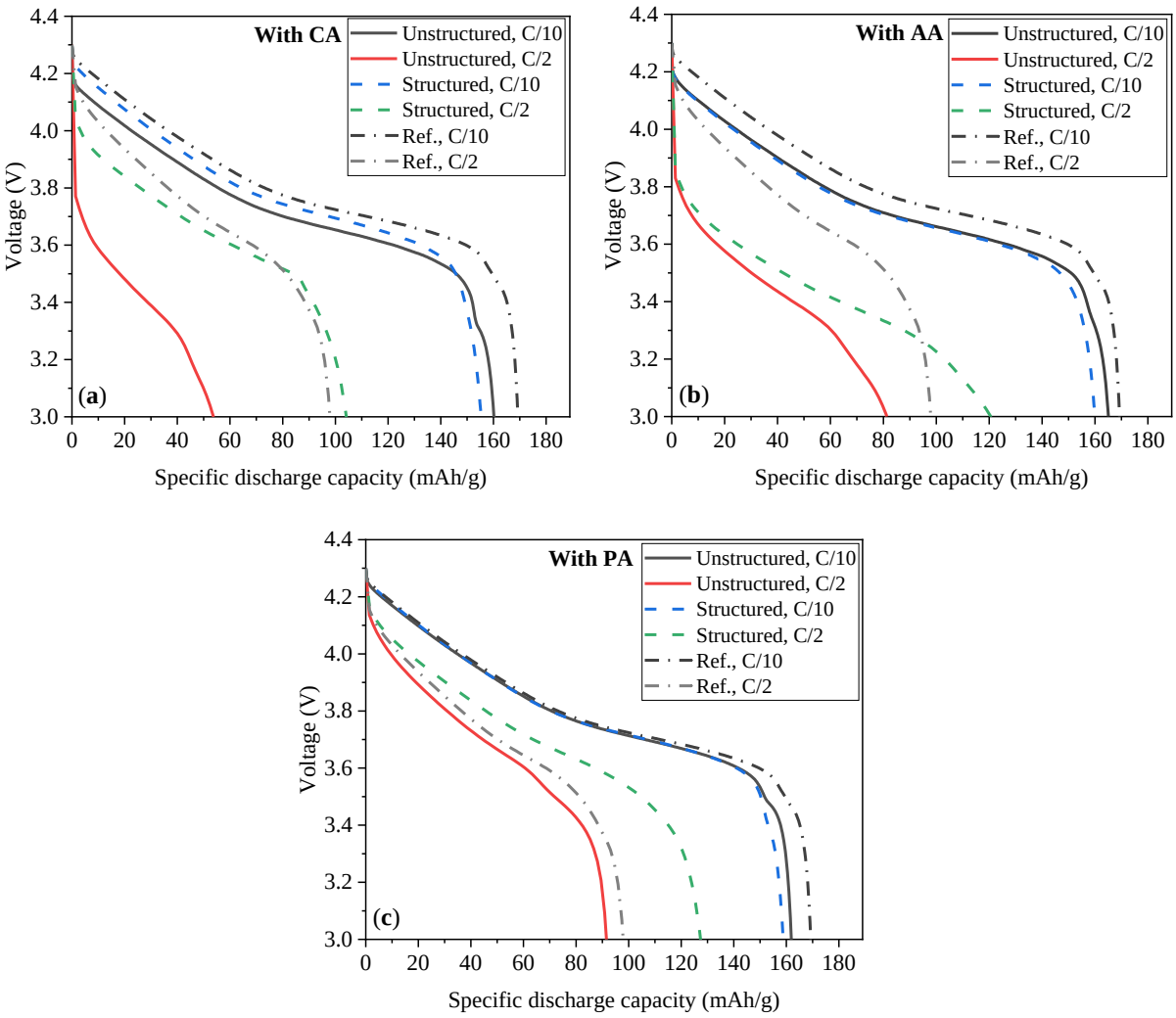

Figure 6. Specific discharge capacity vs. voltage of cells containing unstructured and structured thick-film electrodes with addition of (**a**) CA, (**b**) AA, (**c**) PA, in comparison to the reference cell (Ref.) with PVDF binder at C/10 and C/2.

3.3.2 Long-term performance

After rate capability analysis, the cells were cycled at C/2 in order to study the long-term performance. Figure 7-a displays that cells with PVDF and with PA maintain the highest specific discharge capacities with 88.3 % and 79.8 % after 100 cycles, while cells containing aqueous processed electrodes with addition of CA and AA suffer severe degradation, providing less than 20 % of initial capacity at the end. The strong capacity fading of cells with CA and AA can be resulted from crack formation and the isolation of grains within the primary particles, since they no longer contribute to the electrochemical performance due to loss of electrical connectivity [79]. Sun et al. [80] proposed that the fragmentation of NMC secondary particles after long-term cycling is induced by the strain and strain gradients that arise in a secondary particle due to lithium-ion diffusion. The decohered primary particles participate no longer in electrochemical reaction and thus lead to capacity fading. Since the slurry pH values with different acids were kept the same and the electrode porosity after calendering was adjusted to 35 %, the effect of porosity and mass loading on the electrochemical performance can be excluded [78]. Thus the interaction between acid and NMC 622 particles as well as binder has decisive impact on the electrochemical performance. First of all, cross-linking

reaction can occurred by adding phosphoric acid and citric acid into the slurry with Na-CMC binder, the mechanism is proposed by Kazzazi et al. [67] and Kuenzel et al. [31]. The cross-linked CMC polymers enable a homogenous cover of active material particle surface and a better mechanical integrity of electrodes. The stiff cross-linked CMC binder, especially PA with short molecule, can presumably provide stress on the secondary particles during cycling and alleviate the separation of primary particles. However, the cross-linking might not be the dominant factor for electrochemical performance of electrodes, since the capacity retention of cells with PA electrode is 65 % higher than the ones with CA after 100 cycles. Therefore, the interaction of acid with NMC 622 particles should be taken into account. XPS analysis had proven the existence of phosphates on electrode surface with PA addition, and now combing with the electrochemical performance, it can be concluded that there are not only dried phosphoric acids in the electrode, but also a protective layer composed of phosphate formed and attached to the surface of NMC 622 particles. This protective layer can on the one side mitigate the lithium leaching from NMC 622 surface, and on the other side can prevent the cracking of secondary particles during long-term cycling. Besides, other study shows that the capacity retention of cells with NMC 111 modified with 1 wt. % PA addition is higher in comparison to ones with formic acid or without acid [68], which is consistent with results in the present work.

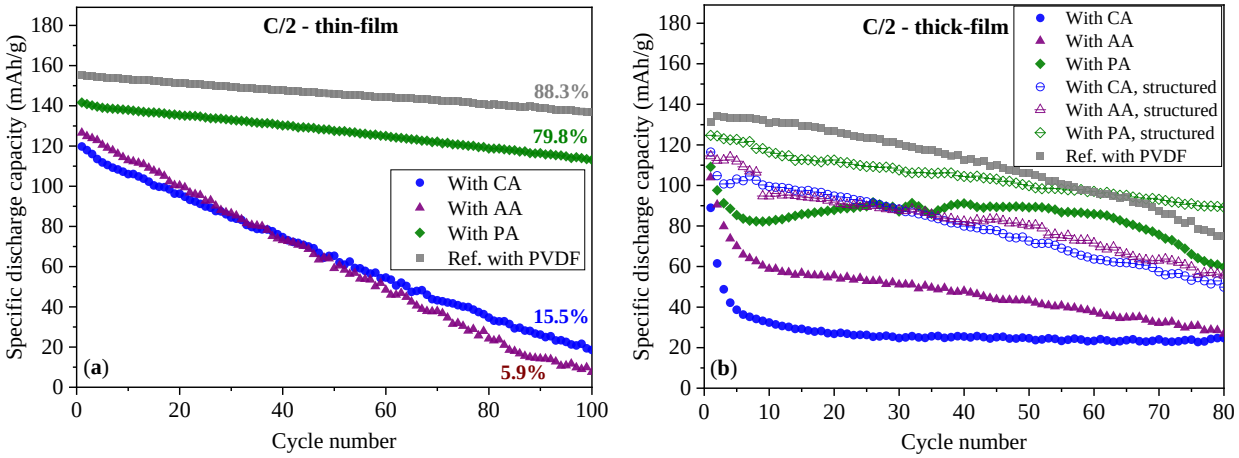

Figure 7. Long-term electrochemical performance of cells containing (**a**) thin-film and (**b**) thick-film NMC 622 cathodes produced with different acid during mixing process at C/2.

Discharge capacities of cells with thick-film electrodes are shown in Figure 7-b. Cells with high mass loaded electrodes exhibit severe capacity drop in comparison to cells with standard loaded electrodes, especially for cells with CA and AA, which lose almost 50 % of initial capacity within the first 10 cycles at C/2. In contrast, cells with PVDF and with PA retain much higher capacity after 80 cycles. The serious capacity loss of cells with thick-film electrodes comes from reaction inhomogeneity owing to the accumulated lithium-ion transport limitation and locally increased ohmic resistance [81]. This means that NMC 622 particles at the bottom cannot reach the same state-of-charge (SOC) as the NMC 622 particles which are near the interface between electrode and electrolyte. Thus the NMC 622 particles close to the Al current collector take no longer part in the electrochemical reaction and remain at the same SOC regardless of charging or discharging. With laser patterning, 3D architectures with channels are generated inside electrodes down to the current collector. The diffusion pathway of lithium-ions to the NMC 622 particles at the bottom is no longer through the whole film but from the side-wall of channel structures into the electrode. This is verified by Smyrek et al. [82] and Zheng et al. [83] using laser induced breakdown spectroscopy (LIBS), whose studies show that laser generated sidewalls provide new lithium-ion diffusion pathways from the liquid electrolyte into the active materials, i.e., the lithium concentration in cycled 3D thick-film electrodes becomes more homogeneous in comparison to unstructured electrodes. Thus, more NMC 622

particles at the bottom of laser patterned thick-film electrodes (in the near of current collector) can actively participate in the electrochemical reaction, because the lithium-ion diffusion can take place through the generated vertical interfaces between electrode and electrolyte. The initial and final specific discharge capacities as well as capacity retention of all cells are summarized in Table 4. It is found that all cells with structured electrodes display both higher initial and final capacity in comparison to ones with unstructured electrodes. Besides, the degradation of cells with structured electrodes during long-term cycling is mitigated, and a sudden capacity drop within the first 10 cycles can be avoided for all cells with structured electrodes. Another important fact is that the cells containing structured electrodes with PA show 13 mAh/g higher capacity in contrast to reference cells with state-of-the-art PVDF binder, holding 72 % capacity after 80 cycles.

Table 4. Initial capacity and capacity after long-term cycling of cells with different types of thick-film electrodes in Figure 7.

	With CA, unstructured	With AA, unstructured	With PA, unstructured	With CA, structured	With AA, structured	With PA, structured	Ref. with PVDF
Initial capacity (mAh/g)	89	104	109	116	114	125	131
Final capacity (mAh/g)	25	29	61	51	57	90	77
Capacity retention (%)	28	28	56	44	50	72	57

3.3.3 EIS analyses

Figure 8 displays Nyquist plots of cells containing unstructured and structured electrodes with different acid addition and the reference cells with PVDF. A Nyquist plot consists of two semicircles at high frequency and a tail at lower frequency. The first small semicircle at high frequency is attributed to the surface resistance of solid electrolyte interphase (SEI), while the second large semicircle from high to mid frequency is owing to the charge transfer resistance of the electrode [84]. The equivalent circuit model for fitting is shown in Figure 8. R_e represents the bulk resistance from current collector, separator, cell case and the electrolyte, while R_{SEI} and a constant phase element CPE_{SEI} are applied on behalf of the resistance contribution of SEI. CPE_{dl} and R_{ct} correspond to the double-layer capacitance and charge transfer resistance, which are owing to the charge transfer behavior between electrolyte and the electrode. The Warburg element (W) in parallel with CPE represent the lithium-ion diffusion in electrolyte and active material [85].

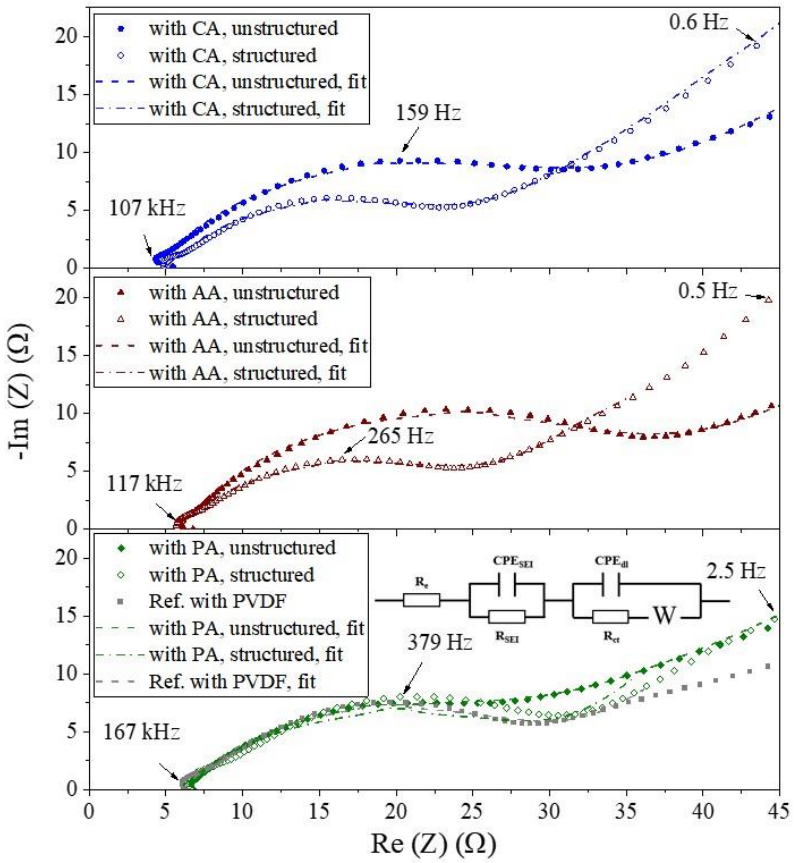

Figure 8. The Nyquist plots of cells containing thick-film cathodes with different acid addition at OCV after rate capability analyses and the fitting curves using equivalent circuit model.

The fitted bulk resistance R_e, SEI resistance R_{SEI} and charge transfer resistance R_{ct} of cells with different types of electrodes are listed in Table 5. All cells show similar values in the bulk resistances as expected, since separator, current collector and other cell components are the same for every cell. The SEI resistance of cells with structured electrodes is similar in comparison to ones with unstructured electrodes, which means that the laser structuring has no negative impact on the formation and the stability of SEI. However, half cells were used in this work, thus we cannot exclude whether there is an impact of laser structuring on the SEI formation on the anode side in full cells. This will be further investigated in future works. The significant difference is observed in the charge transfer resistance. All cells with aqueous processed electrodes exhibit higher charge transfer resistance in contrast to reference cell with PVDF. This might be due to the reduced contact between active material particles with conductive agent and particles with current collector, since a reduced adhesion strength for aqueous processed electrodes is reported [26]. Furthermore, cells with structured electrodes show lower R_{ct} in comparison to ones with unstructured electrode, which might be owing to a larger contact area between electrolyte and particles for laser structured electrodes.

Table 5. The bulk resistance, SEI resistance and charge transfer resistance of cells with different types of electrodes.

	With CA, unstructured	With AA, unstructured	With PA, unstructured	With CA, structured	With AA, structured	With PA, structured	Ref. with PVDF
R_e (Ω)	4.3	6.0	6.4	5.0	5.6	5.9	6.2
R_{SEI} (Ω)	0.4	0.6	0.3	0.5	0.4	0.8	0.7
R_{ct} (Ω)	28.5	29.5	25.4	19.5	21.2	21.6	24.5

3.3.4 CV measurement

CV was performed to investigate the impact of different acid addition on the electrochemical performance of the NMC 622 electrodes. The specific currents of cells with different thick-film electrodes are plotted versus voltage in Figure 9. Only one anodic and cathodic peak is observed in all diagrams, which corresponds to the redox reaction of $Ni^{2+}/Ni^{3+}/Ni^{4+}$ [86] and a phase change from monoclinic to a hexagonal phase (discharge) [38]. This indicates that the acid addition and laser ablation show no impact on the electrochemical properties of NMC 622. Besides, the anodic peak (oxidation) is 1.2-1.5 times higher than the corresponding cathodic peak (reduction). The anodic peak shifts to higher potential with increasing scan rate (ν), while the cathodic peak moves to the opposite direction. The increase of peak-potential separation implies an increasing cell polarization. Furthermore, since the de-/intercalation of lithium-ions from/in NMC 622 electrode is a diffusion-controlled process, the effective diffusion coefficient of lithium-ions D_{eff} can be calculated using $Ip\,m = 0.4463 \cdot (\frac{F^3}{R \cdot T})^{1/2} \cdot A_m \cdot C_0 \cdot D_{eff}^{1/2} \cdot \nu^{1/2}$

Equation 1, which is originated from the Randles-Ševčík equation [87]:

$$\frac{I_p}{m} = 0.4463 \cdot (\frac{F^3}{R \cdot T})^{1/2} \cdot A_m \cdot C_0 \cdot D_{eff}^{1/2} \cdot \nu^{1/2} \qquad \text{Equation 1}$$

where I_p [A] is the peak current from CV, m [g] is the active mass of electrode, F [C/mol] is Faraday's constant, R [J/mol·K] is gas constant, T [K] is the temperature, A_m [cm^2/g] is the electrode area per unit mass, and C_0 [mol/cm^3] is the total amount of lithium-ions in a lithiated NMC 622 particle. In this work, 2/3 of the BET surface area of NMC 622 powder measured by nitrogen adsorption is used as A_m, since the diffusion pathways of lithium-ions in NMC 622 particles are 2-dimensional [8].

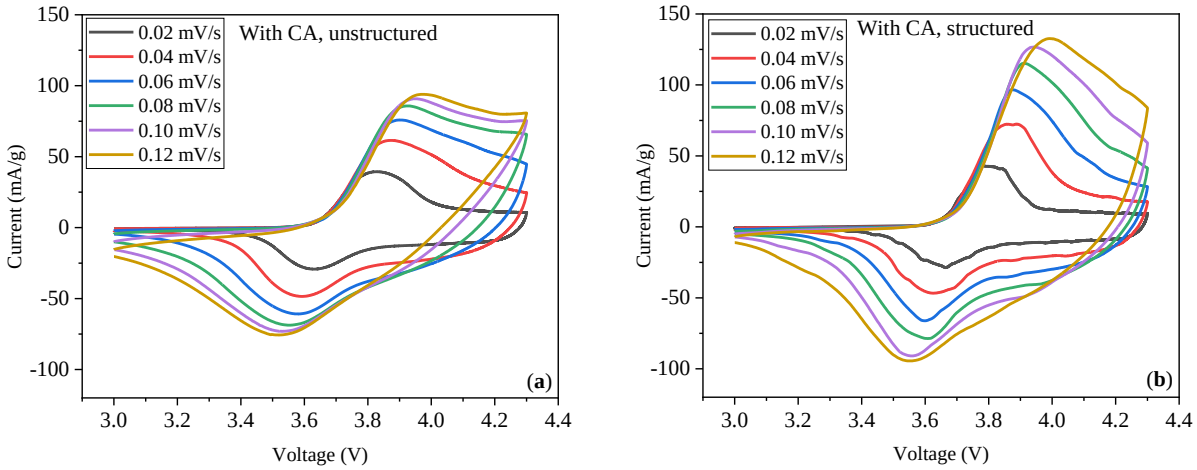

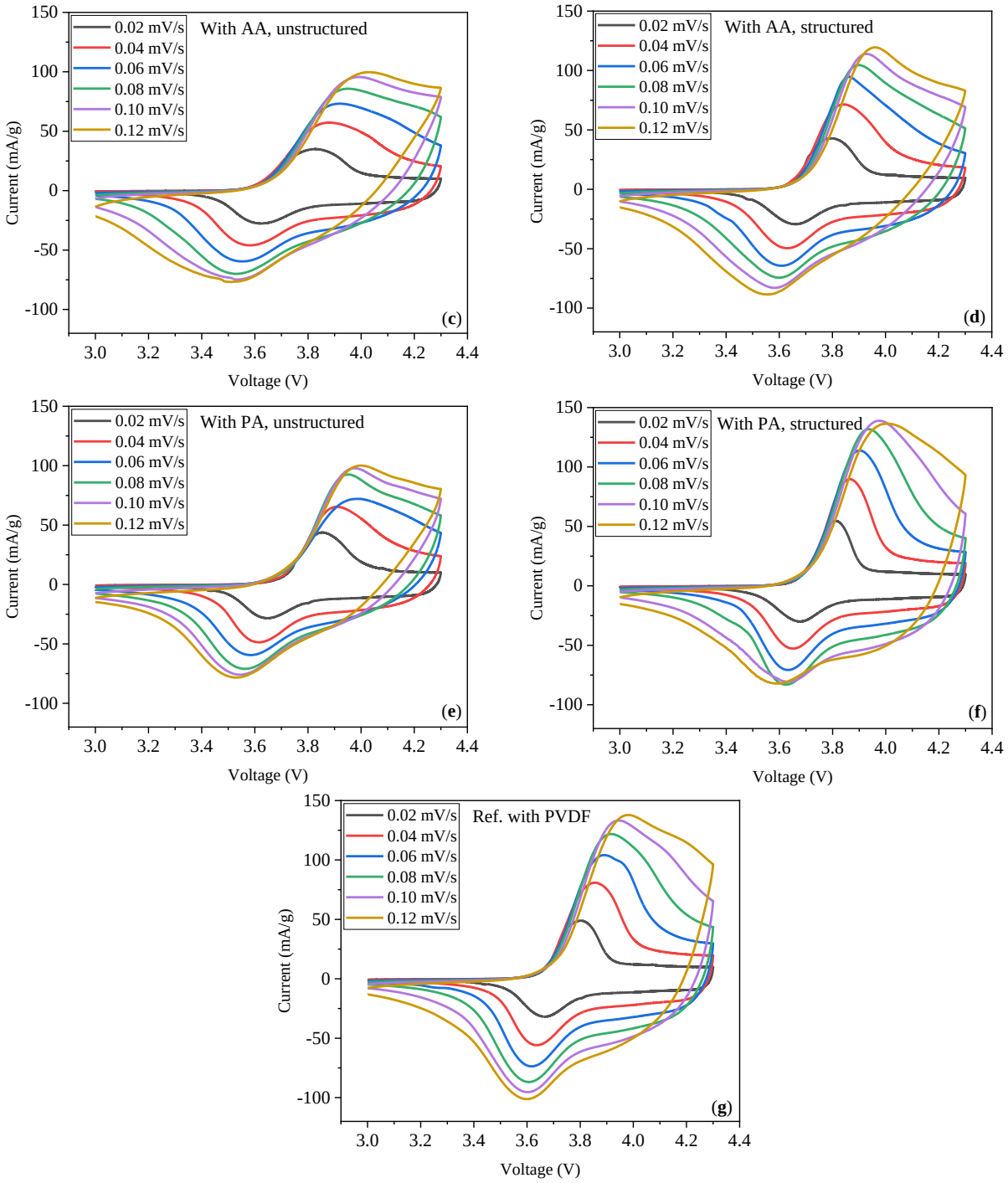

Figure 9. Cyclic voltammetry plots of cells containing unstructured cathodes produced with addition of (**a**) CA, (**c**) AA, and (**e**) PA, and cells with structured electrodes with (**b**) CA, (**d**) AA, and (**f**) PA. In addition, CV plots of reference cell (**g**) with PVDF binder.

In order to calculate the effective diffusion coefficient, specific peak current of each cell was plotted versus the square root of scan rates, which is shown in Figure S2. A linear relation is found for CV from all cells with scan rates ranging from 0.02 to 0.08 mV/s, while the peak current deviates from fitting with scan rates > 0.1 mV/s. This suggests that cells containing NMC 622 electrodes with 150 µm thickness have a critical scan rate of 0.08 mV/s. The calculated D_{eff} of cells in Figure 9 are summarized in Table 6. The values of reference cell with PVDF are in consistent in the order of magnitude with our previous results

using CV [50], however, the effective diffusion coefficients are lower in comparison to results from others using the same active materials but with galvanostatic intermittent titration technique (GITT) method at room temperature [11,88]. The D_{eff} depends not only on the active material, but also reflects lithium-ions diffusion through the interface between electrode and electrolyte [87]. Table 6 reveals that the D_{eff} is higher during charging than discharging for all cells, indicating a faster lithium deintercalation in NMC 622 than intercalation. Besides, cells with laser structured electrodes show higher D_{eff} for both charging and discharging in comparison to ones with unstructured electrode. This can be verified from the rate capability analyses in Figure 5, where the cells with structured electrodes show higher capacity at C/2 to 2C than cells with unstructured electrodes. The cell with structured PA electrode has higher D_{eff} than reference cell with PVDF during charging, which indicates an enhanced fast charging ability of cells with structured aqueous processed electrode modified with PA addition in comparison to cells with state-of-the-art PVDF binder.

Table 6. The effective diffusion coefficient of cells with different types of electrodes during charging and discharging.

	With CA, unstructured	With AA, unstructured	With PA, unstructured	With CA, structured	With AA, structured	With PA, structured	Ref. with PVDF
D_{eff}-charge (cm^2/s)	6.17×10^{-14}	7.37×10^{-14}	6.71×10^{-14}	1.48×10^{-13}	1.14×10^{-13}	1.70×10^{-13}	1.52×10^{-13}
D_{eff}-discharge (cm^2/s)	4.50×10^{-14}	5.13×10^{-14}	5.02×10^{-14}	7.33×10^{-14}	5.85×10^{-14}	8.13×10^{-14}	8.67×10^{-14}

4. Conclusion

Aqueous processed NMC 622 cathodes with different acid additions during mixing process were manufactured, while PVDF binder with NMP as solvent were applied for reference electrodes. All electrodes were characterized using XPS and Raman spectroscopy. Besides, two different electrode thicknesses were selected to represent electrode thicknesses with regard to state-of-the-art (70 µm) and advanced thick-film approach (150 µm). C 1s spectra from XPS analysis show that no distinct differences in Li_2CO_3 amount in aqueous processed electrodes with different acid additions were observed. However, this might be due to the low content of detected lithium carbonate in the samples. After phosphoric acid addition, new peaks appeared in P 2p spectra, which are assigned to phosphates. Raman spectra of different NMC 622 electrode types revealed two Raman-active modes A_{1g} and E_g. After comparing the ratio of A_{1g}/E_g it comes to the assumption that lithium leaching in electrodes processed with citric acid and acetic acid is more distinct that in electrodes processed with phosphoric acid and reference electrode with PVDF. Thus, combining the results from XPS analysis and Raman spectroscopy, a protective layer consisted of phosphates was formed on the surface of NMC 622 in electrodes with phosphoric acid addition, which can mitigate the lithium leaching during slurry preparation.

After electrode manufacturing, laser patterning was performed on thick-film electrodes with ultrafast laser ablation. Cross-sectional analyses showed that line structures were generated from electrode surface down to the current collector. A mass loss of 7.5 % was achieved for different electrode types. The electrodes were subsequently assembled versus lithium in coin cells and different electrochemical analyses were performed. Rate capability analyses display that cells containing thin-film electrodes with AA show almost the same capacity at C/20 and C/10 in comparison to reference cells with PVDF, while the cells with thin-film electrodes with PA maintain higher discharge capacity from 1C to 3C, which might be due to the protective layer formation on NMC 622 particles. As for electrodes with high mass loading, all cells with structured aqueous processed electrodes show higher capacities (10-30 mAh/g) at C/2 and 1C in contrast to reference cells, especially ones with PA and AA. Besides, cells containing laser patterned electrodes with

PA addition exhibit higher capacity retention and the highest final capacity after 80 cycles at C/2 than cells with other electrode types, including reference cells. The positive effect of combing laser patterning and acid modification on the electrochemical performance are further proved by EIS and CV measurements. On the one hand, EIS analyses display that after rate capability analyses, cells containing aqueous processed electrodes with high loading have higher charge transfer resistance than reference cells with PVDF. However, cells with laser patterned aqueous processed electrodes show the same or lower charge transfer resistance in comparison to reference cells. On the other hand, CV analyses show that the effective diffusion coefficient of lithium-ions in cells with laser patterned electrode is higher for both discharging and charging in comparison to ones with unstructured electrodes. Especially for cells with laser patterned PA electrode, which show higher effective diffusion coefficient during charging and almost the same coefficient during discharging in comparison to reference cells with PVDF.

Author contributions

Penghui Zhu: Conceptualization, Methodology, Validation, Investigation, Resources, Writing – Original draft preparation, Writing – Reviewing and Editing. **Vanessa Trouillet:** Methodology, Investigation, Writing – Reviewing and Editing. **Stefan Heißler:** Methodology, Investigation, Writing – Reviewing and Editing. **Wilhelm Pfleging:** Conceptualization, Resources, Writing – Reviewing and Editing, Supervision, Funding acquisition, Project administration.

Declaration of competing interest

The authors declare no competing financial interests.

Acknowledgments

We are grateful for the help of our colleagues, A. Reif, A. Meyer, H. Besser, M. Kapitz, U. Rist, and Y. Sterzl for their technical support and assistance in laser processing and battery analyses. Special thanks are given to W. Bauer and U. Kaufmann for the equipment support in the slurry preparation.

Funding: This work was funded by the Federal Ministry of Education and Research (BMBF), project NextGen-3DBat, project No. 03XP01798F.

References

[1] M. Armand, P. Axmann, D. Bresser, M. Copley, K. Edström, C. Ekberg, D. Guyomard, B. Lestriez, P. Novák, M. Petranikova, W. Porcher, S. Trabesinger, M. Wohlfahrt-Mehrens, H. Zhang, Lithium-ion batteries – Current state of the art and anticipated developments, Journal of Power Sources 479 (2020) 228708. https://doi.org/10.1016/j.jpowsour.2020.228708.

[2] B. Dunn, H. Kamath, J.-M. Tarascon, Electrical energy storage for the grid: a battery of choices, Science 334 (2011) 928–935.

[3] K. Kubota, M. Dahbi, T. Hosaka, S. Kumakura, S. Komaba, Towards K‐ion and Na‐ion batteries as "beyond Li‐ion", The chemical record 18 (2018) 459–479.

[4] T. Bashir, S.A. Ismail, Y. Song, R.M. Irfan, S. Yang, S. Zhou, J. Zhao, L. Gao, A review of the energy storage aspects of chemical elements for lithium-ion based batteries, Energy Materials (2021). https://doi.org/10.20517/energymater.2021.20.

[5] Y. Ding, Z.P. Cano, A. Yu, J. Lu, Z. Chen, Automotive Li-Ion Batteries: Current Status and Future Perspectives, Electrochem. Energ. Rev. 2 (2019) 1–28. https://doi.org/10.1007/s41918-018-0022-z.

[6] A. Masias, J. Marcicki, W.A. Paxton, Opportunities and Challenges of Lithium Ion Batteries in Automotive Applications, ACS Energy Letters 6 (2021) 621–630. https://doi.org/10.1021/acsenergylett.0c02584.
[7] Z.P. Cano, D. Banham, S. Ye, A. Hintennach, J. Lu, M. Fowler, Z. Chen, Batteries and fuel cells for emerging electric vehicle markets, Nature Energy 3 (2018) 279–289. https://doi.org/10.1038/s41560-018-0108-1.
[8] Christian M. Julien, Alain Mauger, Karim Zaghib, Henri Groult, Comparative Issues of Cathode Materials for Li-Ion Batteries.
[9] R. Schmuch, R. Wagner, G. Hörpel, T. Placke, M. Winter, Performance and cost of materials for lithium-based rechargeable automotive batteries, Nat Energy 3 (2018) 267–278. https://doi.org/10.1038/s41560-018-0107-2.
[10] J.-H. Kim, K.-J. Park, S.J. Kim, C.S. Yoon, Y.-K. Sun, A method of increasing the energy density of layered Ni-rich $Li[Ni_{1-2x}Co_xMn_x]O_2$ cathodes (x = 0.05, 0.1, 0.2), J. Mater. Chem. A 7 (2019) 2694–2701. https://doi.org/10.1039/C8TA10438G.
[11] H.-J. Noh, S. Youn, C.S. Yoon, Y.-K. Sun, Comparison of the structural and electrochemical properties of layered $Li[Ni_xCo_yMn_z]O_2$ (x = 1/3, 0.5, 0.6, 0.7, 0.8 and 0.85) cathode material for lithium-ion batteries, Journal of Power Sources 233 (2013) 121–130. https://doi.org/10.1016/j.jpowsour.2013.01.063.
[12] X. Wang, Y.-L. Ding, Y.-P. Deng, Z. Chen, Ni-Rich/Co-Poor Layered Cathode for Automotive Li-Ion Batteries: Promises and Challenges, Adv. Energy Mater. 10 (2020) 1903864. https://doi.org/10.1002/aenm.201903864.
[13] R. Demiryürek, N. Gürbüz, G. Hatipoglu, M. Er, H. Malkoc, O. Guleryuz, G. Uyar, D. Uzun, M.N. Ateş, Roll-to-roll manufacturing method of aqueous-processed thick $LiNi_{0.5}Mn_{0.3}Co_{0.2}O_2$ electrodes for lithium-ion batteries, Intl J of Energy Research 45 (2021) 21182–21194. https://doi.org/10.1002/er.7171.
[14] D.L. Wood, J. Li, C. Daniel, Prospects for reducing the processing cost of lithium ion batteries, Journal of Power Sources 275 (2015) 234–242. https://doi.org/10.1016/j.jpowsour.2014.11.019.
[15] W.B. Hawley, J. Li, Electrode manufacturing for lithium-ion batteries—Analysis of current and next generation processing, Journal of Energy Storage 25 (2019) 100862. https://doi.org/10.1016/j.est.2019.100862.
[16] Y. Zheng, H.J. Seifert, H. Shi, Y. Zhang, C. Kübel, W. Pfleging, 3D silicon/graphite composite electrodes for high-energy lithium-ion batteries, Electrochimica Acta 317 (2019) 502–508. https://doi.org/10.1016/j.electacta.2019.05.064.
[17] A. Meyer, F. Ball, W. Pfleging, The Effect of Silicon Grade and Electrode Architecture on the Performance of Advanced Anodes for Next Generation Lithium-Ion Cells, Nanomaterials (Basel) 11 (2021). https://doi.org/10.3390/nano11123448.
[18] C.-C. Li, J.-T. Lee, Y.-L. Tung, C.-R. Yang, Effects of pH on the dispersion and cell performance of $LiCoO_2$ cathodes based on the aqueous process, J Mater Sci 42 (2007) 5773–5777. https://doi.org/10.1007/s10853-006-1172-7.
[19] J. Li, B.L. Armstrong, J. Kiggans, C. Daniel, D.L. Wood, Lithium ion cell performance enhancement using aqueous $LiFePO_4$ cathode dispersions and polyethyleneimine dispersant, J. Electrochem. Soc. 160 (2012) A201.
[20] Jin-Hyon Lee, Jeom-Soo Kim, Yoon Chang Kim, Dong Sik Zang, Young-Min Choi, Won Il Park, Ungyu Paik, Effect of Carboxymethyl Cellulose on Aqueous Processing of $LiFePO_4$ Cathodes and Their Electrochemical Performance, Electrochemical and Solid-State Letters 11 (2008) A175. https://doi.org/10.1149/1.2966286.

[21] F.A. Çetinel, W. Bauer, Processing of water-based $LiNi_{1/3}Mn_{1/3}Co_{1/3}O_2$ pastes for manufacturing lithium ion battery cathodes, Bulletin of Materials Science 37 (2014) 1685–1690.
[22] Z. Chen, G.-T. Kim, D. Chao, N. Loeffler, M. Copley, J. Lin, Z. Shen, S. Passerini, Toward greener lithium-ion batteries: Aqueous binder-based $LiNi_{0.4}Co_{0.2}Mn_{0.4}O_2$ cathode material with superior electrochemical performance, Journal of Power Sources 372 (2017) 180–187. https://doi.org/10.1016/j.jpowsour.2017.10.074.
[23] M. Bichon, D. Sotta, N. Dupré, E. de Vito, A. Boulineau, W. Porcher, B. Lestriez, Study of Immersion of $LiNi_{0.5}Mn_{0.3}Co_{0.2}O_2$ Material in Water for Aqueous Processing of Positive Electrode for Li-Ion Batteries, ACS Appl. Mater. Interfaces 11 (2019) 18331–18341. https://doi.org/10.1021/acsami.9b00999.
[24] N. Loeffler, J. von Zamory, N. Laszczynski, I. Doberdo, G.-T. Kim, S. Passerini, Performance of $LiNi_{1/3}Mn_{1/3}Co_{1/3}O_2$/graphite batteries based on aqueous binder, Journal of Power Sources 248 (2014) 915–922. https://doi.org/10.1016/j.jpowsour.2013.10.018.
[25] L. Neidhart, K. Fröhlich, N. Eshraghi, D. Cupid, F. Winter, M. Jahn, Aqueous Manufacturing of Defect-Free Thick Multi-Layer NMC811 Electrodes, Nanomaterials (Basel) 12 (2022). https://doi.org/10.3390/nano12030317.
[26] W. Bauer, F.A. Çetinel, M. Müller, U. Kaufmann, Effects of pH control by acid addition at the aqueous processing of cathodes for lithium ion batteries, Electrochimica Acta 317 (2019) 112–119. https://doi.org/10.1016/j.electacta.2019.05.141.
[27] R. Demiryürek, N. Gürbüz, G. Hatipoglu, M. Er, H. Malkoc, O. Guleryuz, G. Uyar, D. Uzun, M.N. Ateş, Roll-to-roll manufacturing method of aqueous-processed thick $LiNi_{0.5}Mn_{0.3}Co_{0.2}O_2$ electrodes for lithium-ion batteries, Intl J of Energy Research 45 (2021) 21182–21194. https://doi.org/10.1002/er.7171.
[28] A. Kukay, R. Sahore, A. Parejiya, W. Blake Hawley, J. Li, D.L. Wood, Aqueous Ni-rich-cathode dispersions processed with phosphoric acid for lithium-ion batteries with ultra-thick electrodes, J. Colloid Interface Sci. 581 (2021) 635–643. https://doi.org/10.1016/j.jcis.2020.07.144.
[29] D.V. Carvalho, N. Loeffler, M. Hekmatfar, A. Moretti, G.-T. Kim, S. Passerini, Evaluation of guar gum-based biopolymers as binders for lithium-ion batteries electrodes, Electrochimica Acta 265 (2018) 89–97. https://doi.org/10.1016/j.electacta.2018.01.083.
[30] L. Ibing, T. Gallasch, P. Schneider, P. Niehoff, A. Hintennach, M. Winter, F.M. Schappacher, Towards water based ultra-thick Li ion battery electrodes – A binder approach, Journal of Power Sources 423 (2019) 183–191. https://doi.org/10.1016/j.jpowsour.2019.03.020.
[31] M. Kuenzel, D. Bresser, T. Diemant, D.V. Carvalho, G.-T. Kim, R.J. Behm, S. Passerini, Complementary Strategies Toward the Aqueous Processing of High-Voltage $LiNi_{0.5}Mn_{1.5}O_4$Lithium-Ion Cathodes, ChemSusChem 11 (2018) 562–573. https://doi.org/10.1002/cssc.201702021.
[32] I.A. Shkrob, J.A. Gilbert, P.J. Phillips, R. Klie, R.T. Haasch, J. Bareño, D.P. Abraham, Chemical weathering of layered Ni-rich oxide electrode materials: evidence for cation exchange, J. Electrochem. Soc. 164 (2017) A1489.
[33] X. Zhang, W.J. Jiang, X.P. Zhu, A. Mauger, Qilu, C.M. Julien, Aging of $LiNi_{1/3}Mn_{1/3}Co_{1/3}O_2$ cathode material upon exposure to H_2O, Journal of Power Sources 196 (2011) 5102–5108. https://doi.org/10.1016/j.jpowsour.2011.02.009.
[34] J.-h. Park, J.-k. Park, J.-w. Lee, Stability of $LiNi_{0.6}Mn_{0.2}Co_{0.2}O_2$ as a Cathode Material for Lithium-Ion Batteries against Air and Moisture, Bull. Korean Chem. Soc. 37 (2016) 344–348. https://doi.org/10.1002/bkcs.10679.
[35] Z. Chen, J. Wang, J. Huang, T. Fu, G. Sun, S. Lai, R. Zhou, K. Li, J. Zhao, The high-temperature and high-humidity storage behaviors and electrochemical degradation mechanism of $LiNi_{0.6}Co_{0.2}Mn_{0.2}O_2$

cathode material for lithium ion batteries, Journal of Power Sources 363 (2017) 168–176. https://doi.org/10.1016/j.jpowsour.2017.07.087.
[36] L. Azhari, X. Zhou, B. Sousa, Z. Yang, G. Gao, Y. Wang, Effects of Extended Aqueous Processing on Structure, Chemistry, and Performance of Polycrystalline $LiNi_xMn_yCo_zO_2$ Cathode Powders, ACS Appl. Mater. Interfaces 12 (2020) 57963–57974. https://doi.org/10.1021/acsami.0c20105.
[37] W.B. Hawley, A. Parejiya, Y. Bai, H.M. Meyer, D.L. Wood, J. Li, Lithium and transition metal dissolution due to aqueous processing in lithium-ion battery cathode active materials, Journal of Power Sources 466 (2020) 228315. https://doi.org/10.1016/j.jpowsour.2020.228315.
[38] M. Hofmann, M. Kapuschinski, U. Guntow, G.A. Giffin, Implications of Aqueous Processing for High Energy Density Cathode Materials: Part I. Ni-Rich Layered Oxides, J. Electrochem. Soc. 167 (2020) 140512. https://doi.org/10.1149/1945-7111/abc033.
[39] S.Y. Li, B.C. Church, Effect of aqueous-based cathode slurry pH and immersion time on corrosion of aluminum current collector in lithium-ion batteries, Materials and Corrosion 67 (2016) 978–987. https://doi.org/10.1002/maco.201608843.
[40] M. Wood, J. Li, R.E. Ruther, Z. Du, E.C. Self, H.M. Meyer, C. Daniel, I. Belharouak, D.L. Wood, Chemical stability and long-term cell performance of low-cobalt, Ni-Rich cathodes prepared by aqueous processing for high-energy Li-Ion batteries, Energy Storage Materials 24 (2020) 188–197. https://doi.org/10.1016/j.ensm.2019.08.020.
[41] K. Notake, T. Gunji, H. Kokubun, S. Kosemura, Y. Mochizuki, T. Tanabe, S. Kaneko, S. Ugawa, H. Lee, F. MATSUMOTO, The application of a water-based hybrid polymer binder to a high-voltage and high-capacity Li-rich solid-solution cathode and its performance in Li-ion batteries, J Appl Electrochem 46 (2016) 267–278. https://doi.org/10.1007/s10800-016-0930-8.
[42] T. Tanabe, T. Gunji, Y. Honma, K. Miyamoto, T. Tsuda, Y. Mochizuki, S. Kaneko, S. Ugawa, H. Lee, T. Ohsaka, F. MATSUMOTO, Preparation of Water-Resistant Surface Coated High-Voltage LiNi0.5Mn1.5O4 Cathode and Its Cathode Performance to Apply a Water-Based Hybrid Polymer Binder to Li-Ion Batteries, Electrochimica Acta 224 (2017) 429–438. https://doi.org/10.1016/j.electacta.2016.12.064.
[43] I. Doberdò, N. Löffler, N. Laszczynski, D. Cericola, N. Penazzi, S. Bodoardo, G.-T. Kim, S. Passerini, Enabling aqueous binders for lithium battery cathodes – Carbon coating of aluminum current collector, Journal of Power Sources 248 (2014) 1000–1006. https://doi.org/10.1016/j.jpowsour.2013.10.039.
[44] M. Kuenzel, D. Bresser, G.-T. Kim, P. Axmann, M. Wohlfahrt-Mehrens, S. Passerini, Unveiling and Amplifying the Benefits of Carbon-Coated Aluminum Current Collectors for Sustainable LiNi 0.5 Mn 1.5 O 4 Cathodes, ACS Appl. Energy Mater. 3 (2020) 218–230. https://doi.org/10.1021/acsaem.9b01302.
[45] K. Sahni, M. Ashuri, Q. He, R. Sahore, I.D. Bloom, Y. Liu, J.A. Kaduk, L.L. Shaw, H_3PO_4 treatment to enhance the electrochemical properties of $Li(Ni_{1/3}Mn_{1/3}Co_{1/3})O_2$ and $Li(Ni_{0.5}Mn_{0.3}Co_{0.2})O_2$ cathodes, Electrochimica Acta 301 (2019) 8–22. https://doi.org/10.1016/j.electacta.2019.01.153.
[46] K.-Y. Park, J.-W. Park, W.M. Seong, K. Yoon, T.-H. Hwang, K.-H. Ko, J.-H. Han, Y. Jaedong, K. Kang, Understanding capacity fading mechanism of thick electrodes for lithium-ion rechargeable batteries, Journal of Power Sources 468 (2020) 228369. https://doi.org/10.1016/j.jpowsour.2020.228369.
[47] W. Pfleging, A review of laser electrode processing for development and manufacturing of lithium-ion batteries, Nanophotonics 7 (2018) 549–573. https://doi.org/10.1515/nanoph-2017-0044.
[48] W. Pfleging, Recent progress in laser texturing of battery materials: A review of tuning electrochemical performances, related material development, and prospects for large-scale manufacturing, International Journal of Extreme Manufacturing 3 (2020) 12002.

[49] W. Pfleging, J. Pröll, A new approach for rapid electrolyte wetting in tape cast electrodes for lithium-ion batteries, J. Mater. Chem. A 2 (2014) 14918–14926. https://doi.org/10.1039/C4TA02353F.
[50] P. Zhu, H.J. Seifert, W. Pfleging, The ultrafast laser ablation of $Li(Ni_{0.6}Mn_{0.2}Co_{0.2})O_2$ electrodes with high mass loading, Applied Sciences 9 (2019) 4067.
[51] Z. Song, P. Zhu, W. Pfleging, J. Sun, Electrochemical performance of thick-film $Li(Ni_{0.6}Mn_{0.2}Co_{0.2})O_2$ cathode with hierarchic structures and laser ablation, Nanomaterials (Basel) 11 (2021) 2962.
[52] J. Park, S. Hyeon, S. Jeong, H.-J. Kim, Performance enhancement of Li-ion battery by laser structuring of thick electrode with low porosity, Journal of Industrial and Engineering Chemistry 70 (2019) 178–185.
[53] N. Dunlap, D.B. Sulas-Kern, P.J. Weddle, F. Usseglio-Viretta, P. Walker, P. Todd, D. Boone, A.M. Colclasure, K. Smith, B.J. Tremolet de Villers, D.P. Finegan, Laser ablation for structuring Li-ion electrodes for fast charging and its impact on material properties, rate capability, Li plating, and wetting, Journal of Power Sources 537 (2022) 231464. https://doi.org/10.1016/j.jpowsour.2022.231464.
[54] J. Park, C. Jeon, W. Kim, S.-J. Bong, S. Jeong, H.-J. Kim, Challenges, laser processing and electrochemical characteristics on application of ultra-thick electrode for high-energy lithium-ion battery, Journal of Power Sources 482 (2021) 228948. https://doi.org/10.1016/j.jpowsour.2020.228948.
[55] T. Tsuda, Y. ISHIHARA, T. WATANABE, N. Ando, T. Gunji, N. Soma, S. Nakamura, N. Hayashi, T. Ohsaka, F. MATSUMOTO, An Improved High-rate Discharging Performance of "Unbalanced" $LiFePO_4$ Cathodes with Different $LiFePO_4$ Loadings by a Grid-patterned Micrometer Size-holed Electrode Structuring, Electrochemistry 87 (2019) 370–378. https://doi.org/10.5796/electrochemistry.19-00049.
[56] A. Meyer, Y. Sterzl, S. Xiao, U. Rädel, W. Pfleging (Eds.), Ablation behavior of electrode materials during high power and high repetition rate laser structuring, SPIE, 2022.
[57] R. Dubey, M.-D. Zwahlen, Y. Shynkarenko, S. Yakunin, A. Fuerst, M.V. Kovalenko, K.V. Kravchyk, Laser Patterning of High-Mass-Loading Graphite Anodes for High-Performance Li-Ion Batteries, Batteries & Supercaps 4 (2021) 464–468. https://doi.org/10.1002/batt.202000253.
[58] J. Kriegler, L. Hille, S. Stock, L. Kraft, J. Hagemeister, J.B. Habedank, A. Jossen, M.F. Zaeh, Enhanced performance and lifetime of lithium-ion batteries by laser structuring of graphite anodes, Applied Energy 303 (2021) 117693. https://doi.org/10.1016/j.apenergy.2021.117693.
[59] P. Zhu, J. Han, W. Pfleging, Characterization and laser structuring of aqueous processed $Li(Ni_{0.6}Mn_{0.2}Co_{0.2})O_2$ thick-film cathodes for lithium-ion batteries, Nanomaterials (Basel) 11 (2021) 1840.
[60] J.-H. Rakebrandt, P. Smyrek, Y. Zheng, H.J. Seifert, W. Pfleging (Eds.), Laser processing of thick Li $(NiMnCo)O_2$ electrodes for lithium-ion batteries, SPIE, 2017.
[61] A. Kwade, W. Haselrieder, R. Leithoff, A. Modlinger, F. Dietrich, K. Droeder, Current status and challenges for automotive battery production technologies, Nat Energy 3 (2018) 290–300. https://doi.org/10.1038/s41560-018-0130-3.
[62] J.H. Scofield, Hartree-Slater subshell photoionization cross-sections at 1254 and 1487 eV, Journal of Electron Spectroscopy and Related Phenomena 8 (1976) 129–137.
[63] M.E. Spahr, D. Goers, A. Leone, S. Stallone, E. Grivei, Development of carbon conductive additives for advanced lithium ion batteries, Journal of Power Sources 196 (2011) 3404–3413. https://doi.org/10.1016/j.jpowsour.2010.07.002.

[64] M.E. Spahr, D. Goers, A. Leone, S. Stallone, E. Grivei, Development of carbon conductive additives for advanced lithium ion batteries, Journal of Power Sources 196 (2011) 3404–3413. https://doi.org/10.1016/j.jpowsour.2010.07.002.
[65] N. Hornsveld, B. Put, W.M.M. Kessels, P.M. Vereecken, M. Creatore, Plasma-assisted and thermal atomic layer deposition of electrochemically active Li_2CO_3, RSC Adv. 7 (2017) 41359–41368. https://doi.org/10.1039/C7RA07722J.
[66] A.T. Appapillai, A.N. Mansour, J. Cho, Y. Shao-Horn, Microstructure of $LiCoO_2$ with and without "$AlPO_4$" Nanoparticle Coating: Combined STEM and XPS Studies, Chem. Mater. 19 (2007) 5748–5757. https://doi.org/10.1021/cm0715390.
[67] A. Kazzazi, D. Bresser, A. Birrozzi, J. von Zamory, M. Hekmatfar, S. Passerini, Comparative Analysis of Aqueous Binders for High-Energy Li-Rich NMC as a Lithium-Ion Cathode and the Impact of Adding Phosphoric Acid, ACS Appl. Mater. Interfaces 10 (2018) 17214–17222. https://doi.org/10.1021/acsami.8b03657.
[68] N. Loeffler, G.-T. Kim, F. Mueller, T. Diemant, J.-K. Kim, R.J. Behm, S. Passerini, In situ coating of Li $[Ni_{0.33}Mn_{0.33}Co_{0.33}]O_2$ particles to enable aqueous electrode processing, ChemSusChem 9 (2016) 1112–1117.
[69] R. Franke, T. Chassé, P. Streubel, A. Meisel, Auger parameters and relaxation energies of phosphorus in solid compounds, Journal of Electron Spectroscopy and Related Phenomena 56 (1991) 381–388. https://doi.org/10.1016/0368-2048(91)85035-R.
[70] I. Hamam, N. Zhang, A. Liu, M.B. Johnson, J.R. Dahn, Study of the Reactions between Ni-Rich Positive Electrode Materials and Aqueous Solutions and their Relation to the Failure of Li-Ion Cells, J. Electrochem. Soc. 167 (2020) 130521. https://doi.org/10.1149/1945-7111/abb9cd.
[71] X. Zhang, A. Mauger, Q. Lu, H. Groult, L. Perrigaud, F. Gendron, C.M. Julien, Synthesis and characterization of $LiNi_{1/3}Mn_{1/3}Co_{1/3}O_2$ by wet-chemical method, Electrochimica Acta 55 (2010) 6440–6449. https://doi.org/10.1016/j.electacta.2010.06.040.
[72] E. Flores, P. Novák, U. Aschauer, E.J. Berg, Cation Ordering and Redox Chemistry of Layered Ni-Rich $Li_xNi_{1-2\,y}Co_yMn_yO_2$: An Operando Raman Spectroscopy Study, Chem. Mater. 32 (2020) 186–194. https://doi.org/10.1021/acs.chemmater.9b03202.
[73] E. Flores, P. Novák, E.J. Berg, In situ and Operando Raman Spectroscopy of Layered Transition Metal Oxides for Li-ion Battery Cathodes, Front. Energy Res. 6 (2018) 5175. https://doi.org/10.3389/fenrg.2018.00082.
[74] C. Julien, Local cationic environment in lithium nickel–cobalt oxides used as cathode materials for lithium batteries, Solid State Ionics 136 (2000) 887–896.
[75] T. Tsuda, N. Ando, K. Matsubara, T. Tanabe, K. Itagaki, N. Soma, S. Nakamura, N. Hayashi, T. Gunji, T. Ohsaka, Improvement of high-rate charging/discharging performance of a lithium ion battery composed of laminated LiFePO4 cathodes/graphite anodes having porous electrode structures fabricated with a pico-second pulsed laser, Electrochimica Acta 291 (2018) 267–277.
[76] K. Edström, T. Gustafsson, J.O. Thomas, The cathode–electrolyte interface in the Li-ion battery, Electrochimica Acta 50 (2004) 397–403. https://doi.org/10.1016/j.electacta.2004.03.049.
[77] C.-H. Jo, D.-H. Cho, H.-J. Noh, H. Yashiro, Y.-K. Sun, S.T. Myung, An effective method to reduce residual lithium compounds on Ni-rich Li[Ni0.6Co0.2Mn0.2]O2 active material using a phosphoric acid derived Li3PO4 nanolayer, Nano Res. 8 (2015) 1464–1479. https://doi.org/10.1007/s12274-014-0631-8.
[78] C. Heubner, A. Nickol, J. Seeba, S. Reuber, N. Junker, M. Wolter, M. Schneider, A. Michaelis, Understanding thickness and porosity effects on the electrochemical performance of LiNi0.6Co0.2Mn0.2O2-based cathodes for high energy Li-ion batteries, Journal of Power Sources 419 (2019) 119–126. https://doi.org/10.1016/j.jpowsour.2019.02.060.

[79] D.J. Miller, C. Proff, J.G. Wen, D.P. Abraham, J. Bareño, Observation of Microstructural Evolution in Li Battery Cathode Oxide Particles by In Situ Electron Microscopy, Adv. Energy Mater. 3 (2013) 1098–1103. https://doi.org/10.1002/aenm.201300015.
[80] G. Sun, T. Sui, B. Song, H. Zheng, L. Lu, A.M. Korsunsky, On the fragmentation of active material secondary particles in lithium ion battery cathodes induced by charge cycling, Extreme Mechanics Letters 9 (2016) 449–458. https://doi.org/10.1016/j.eml.2016.03.018.
[81] K.-Y. Park, J.-W. Park, W.M. Seong, K. Yoon, T.-H. Hwang, K.-H. Ko, J.-H. Han, Y. Jaedong, K. Kang, Understanding capacity fading mechanism of thick electrodes for lithium-ion rechargeable batteries, Journal of Power Sources 468 (2020) 228369. https://doi.org/10.1016/j.jpowsour.2020.228369.
[82] P. Smyrek, T. Bergfeldt, H.J. Seifert, W. Pfleging, Laser-induced breakdown spectroscopy for the quantitative measurement of lithium concentration profiles in structured and unstructured electrodes, J. Mater. Chem. A 7 (2019) 5656–5665. https://doi.org/10.1039/C8TA10328C.
[83] Y. Zheng, L. Pfäffl, H.J. Seifert, W. Pfleging, Lithium distribution in structured graphite anodes investigated by laser-induced breakdown spectroscopy, Applied Sciences 9 (2019) 4218.
[84] L. Wang, J. Zhao, X. He, J. Gao, J. Li, C. Wan, C. Jiang, Electrochemical impedance spectroscopy (EIS) study of $LiNi_{1/3}Co_{1/3}Mn_{1/3}O_2$ for Li-ion batteries, Int. J. Electrochem. Sci 7 (2012) 345–353.
[85] J.-M. Atebamba, J. Moskon, S.P. Pejovnik, M. Gaberscek, On the Interpretation of Measured Impedance Spectra of Insertion Cathodes for Lithium-Ion Batteries, J. Electrochem. Soc. 157 (2010) A1218. https://doi.org/10.1149/1.3489353.
[86] Y. Wei, J. Zheng, S. Cui, X. Song, Y. Su, W. Deng, Z. Wu, X. Wang, W. Wang, M. Rao, Y. Lin, C. Wang, K. Amine, F. Pan, Kinetics Tuning of Li-Ion Diffusion in Layered $Li(Ni_xMn_yCo_z)O_2$, J. Am. Chem. Soc. 137 (2015) 8364–8367. https://doi.org/10.1021/jacs.5b04040.
[87] Denis Y. W. Yu, Christopher Fietzek, Wolfgang Weydanz, Kazunori Donoue, Takao Inoue, Hiroshi Kurokawa, Shin Fujitani, Study of $LiFePO_4$ by Cyclic Voltammetry, J. Electrochem. Soc. 154 (2007) A253. https://doi.org/10.1149/1.2434687.
[88] S. Cui, Y. Wei, T. Liu, W. Deng, Z. Hu, Y. Su, H. Li, M. Li, H. Guo, Y. Duan, W. Wang, M. Rao, J. Zheng, X. Wang, F. Pan, Optimized Temperature Effect of Li-Ion Diffusion with Layer Distance in $Li(Ni_xMn_yCo_z)O_2$ Cathode Materials for High Performance Li-Ion Battery, Adv. Energy Mater. 6 (2016) 1501309. https://doi.org/10.1002/aenm.201501309.